

## QUANTUM ELECTRONICS

# Probing Johnson noise and ballistic transport in normal metals with a single-spin qubit

S. Kolkowitz,<sup>1,\*</sup> A. Safira,<sup>1,\*</sup> A. A. High,<sup>1,2</sup> R. C. Devlin,<sup>2</sup> S. Choi,<sup>1</sup> Q. P. Unterreithmeier,<sup>1</sup> D. Patterson,<sup>1</sup> A. S. Zibrov,<sup>1</sup> V. E. Manucharyan,<sup>3</sup> H. Park,<sup>1,2†</sup> M. D. Lukin<sup>1,†</sup>

Thermally induced electrical currents, known as Johnson noise, cause fluctuating electric and magnetic fields in proximity to a conductor. These fluctuations are intrinsically related to the conductivity of the metal. We use single-spin qubits associated with nitrogen-vacancy centers in diamond to probe Johnson noise in the vicinity of conductive silver films. Measurements of polycrystalline silver films over a range of distances (20 to 200 nanometers) and temperatures (10 to 300 kelvin) are consistent with the classically expected behavior of the magnetic fluctuations. However, we find that Johnson noise is markedly suppressed next to single-crystal films, indicative of a substantial deviation from Ohm's law at length scales below the electron mean free path. Our results are consistent with a generalized model that accounts for the ballistic motion of electrons in the metal, indicating that under the appropriate conditions, nearby electrodes may be used for controlling nanoscale optoelectronic, atomic, and solid-state quantum systems.

Understanding electron transport, dissipation, and fluctuations at submicrometer length scales is critical for the continued miniaturization of electronic (1, 2) and optical devices (3–5), as well as atom and ion traps (6–10), and for the electrical control of solid-state quantum circuits (11). Although it is well known that electronic transport in small samples defies the conventional wisdom associated with macroscopic devices, resistance-free transport is difficult to observe directly. Most of the measurements demonstrating these effects make use of ohmic contacts attached to submicrometer-scale samples and observe quantized but finite resistance corresponding to the voltage drop at the contact of such a system with a macroscopic conductor (12, 13). Techniques for noninvasive probing of electron transport are being actively explored (14, 15), because they can provide insights into electronic dynamics at small length scales. Our approach makes use of the electromagnetic fluctuations associated with Johnson noise close to a conducting surface, which can be directly linked to the dielectric function at similar length scales, providing a noninvasive probe of electronic transport inside the metal. Measurements of these fluctuations at micrometer length scales with cold, trapped atoms showed excellent agreement with predictions based on diffusive electron motion (7–9), whereas millimeter-length scale measurements with superconducting quantum interference devices (SQUIDs) have been demonstrated for use as an accurate, contact-free thermometer (16).

Our approach makes use of the electronic spin associated with nitrogen-vacancy (NV) defect centers in diamond to study the spectral,

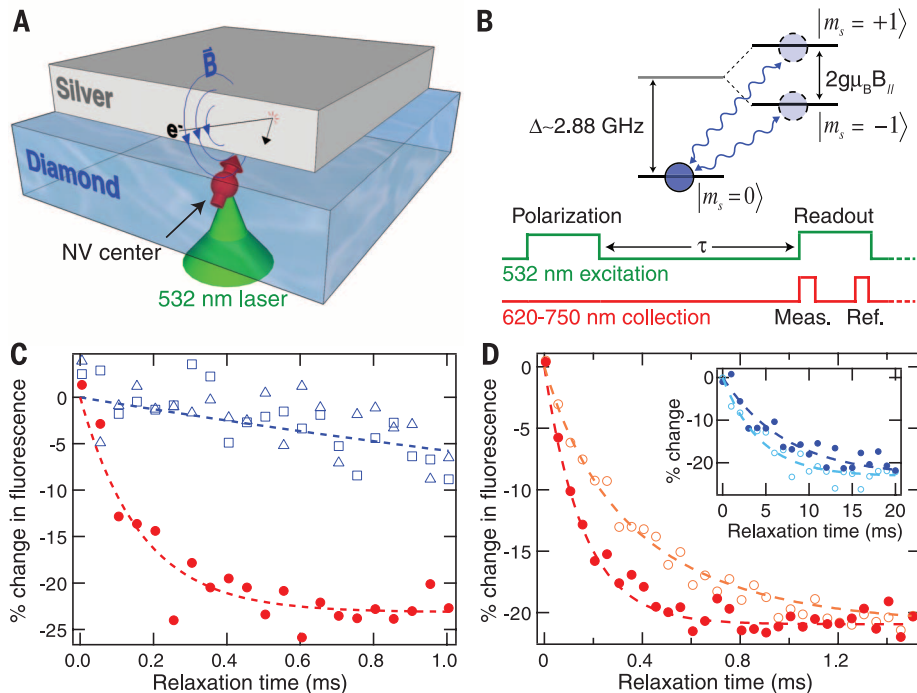


**Fig. 1. Probing Johnson noise with single-spin qubits.** (A) The thermally induced motion of electrons in silver generates fluctuating magnetic fields ( $\vec{B}$ ), which are detected with the spin of a single NV. The NV is polarized and read out through the back side of the diamond. (B) The NV spin is polarized into the  $|m_s = 0\rangle$  state using a green laser pulse. Spin relaxation into the  $|m_s = \pm 1\rangle$  states is induced by magnetic field noise at  $\sim 2.88$  GHz. After wait time  $\tau$ , the population left in  $|m_s = 0\rangle$  is read out by spin-dependent fluorescence. All measurements shown were performed at low magnetic fields ( $\Delta \gg g\mu_B B_{||}/h$ ). (C) Spin relaxation data for the same single shallow-implant NV before silver deposition (open blue squares), with silver deposited (red circles) and after the silver has been removed (open blue triangles). (D) Spin relaxation for a single NV close to a silver film prepared in the  $|m_s = 0\rangle$  state (red circles) and in the  $|m_s = -1\rangle$  state (open orange circles). (Inset) Spin relaxation for a single native NV in bulk diamond in the  $|m_s = 0\rangle$  state (blue circles) and in the  $|m_s = -1\rangle$  state (open light blue circles).

spatial, and temperature dependence of Johnson noise emanating from conductors. The magnetic Johnson noise results in a reduction of the spin lifetime of individual NV electronic spins, thereby allowing us to probe the intrinsic properties of the conductor noninvasively over a wide range of parameters. Individual, optically resolvable NV centers are implanted  $\sim 15$  nm below the surface of a  $\sim 30$ - $\mu\text{m}$ -thick diamond sample. A silver film is then deposited or positioned on the diamond surface (Fig. 1A). The spin sublevels  $|m_s = 0\rangle$  and  $|m_s = \pm 1\rangle$  of the NV electronic ground state exhibit a zero-field splitting of  $\Delta = 2\pi \times 2.88$  GHz (17–20). The relaxation rates between the  $|m_s = 0\rangle$  and  $|m_s = \pm 1\rangle$  states provide a sensitive probe of the magnetic field noise at the transition frequencies  $\omega_{\pm} = \Delta \pm 2g\mu_B B_{||}$ , where  $B_{||}$  is the magnetic field along the NV axis,  $g \approx 2$  is the electron g-factor, and  $\mu_B$  is the Bohr magneton (21, 22) (Fig. 1B).

The impact of Johnson noise emanating from a polycrystalline silver film deposited on the diamond surface (Fig. 1C) is evident when comparing the relaxation of a single NV spin below the silver (red circles) to the relaxation of the same NV before film deposition and after removal of the silver (open blue squares and triangles, respectively). At room temperature and

<sup>1</sup>Department of Physics, Harvard University, Cambridge, MA 02138, USA. <sup>2</sup>Department of Chemistry and Chemical Biology, Harvard University, Cambridge, MA 02138, USA.

<sup>3</sup>Department of Physics, University of Maryland, College Park, MD 20742, USA.

\*These authors contributed equally to this work. †Corresponding author. E-mail: lukin@physics.harvard.edu (M.D.L.); hongkun\_park@harvard.edu (H.P.)

in the absence of external noise, the spin lifetime is limited by phonon-induced relaxation to  $T_1^{\text{ph}} \approx 4$  ms. With the silver nearby, the lifetime of the  $|m_s = 0\rangle$  state is reduced to  $T_1 = 165$   $\mu$ s, which we attribute to magnetic Johnson noise emanating from the film. To verify that the enhanced relaxation is due to magnetic noise, we compare the lifetime of the  $|m_s = 0\rangle$  state, which has magnetic dipole allowed transitions to both of the  $|m_s = \pm 1\rangle$  states, to that of the  $|m_s = -1\rangle$  state, which can only decay directly to the  $|m_s = 0\rangle$  state (Fig. 1D). As expected for relaxation induced by magnetic noise, the  $|m_s = -1\rangle$  state has approximately twice the lifetime of the  $|m_s = 0\rangle$  state (23). This is in contrast to the observed lifetimes when limited by phonon-induced relaxation (Fig. 1D, inset), where the  $|m_s = 0\rangle$  and  $|m_s = \pm 1\rangle$  states have almost identical lifetimes (24). In what follows, we define  $T_1$  as the lifetime of the  $|m_s = 0\rangle$  state.

To test the scaling of Johnson noise with distance ( $d$ ) to the metal, we deposit a layer of  $\text{SiO}_2$  on the diamond surface with a gradually increasing thickness (Fig. 2A). We characterize the thickness of the  $\text{SiO}_2$  layer as a function of position on the sample (Fig. 2B, inset) and deposit a 60-nm polycrystalline silver film on top of the  $\text{SiO}_2$ . The conductivity of the silver film is measured to be  $2.9 \times 10^7$  S/m at room temperature. By measuring the relaxation rates  $\Gamma = 1/T_1$  of individual NVs at different positions along the  $\text{SiO}_2$  ramp, we extract the distance dependence of the noise (Fig. 2B), with the uncertainty in the distance dominated by the variation in the implanted depth of the NVs (taken to be  $15 \pm 10$  nm). To ensure that the measured rates are Johnson noise limited, we measure the spin relaxation of 5 to 10 randomly selected NVs per location along the ramp and plot the minimum observed rate at each location (23). As expected (7–9), the magnitude of the noise increases as the NVs approach the silver surface.

To investigate the dependence of the noise on temperature and conductivity, we deposit a 100-nm polycrystalline silver film on a diamond sample and measure the  $T_1$  of a single NV beneath the silver over a range of temperatures ( $\sim 10$  to 295 K). The measured relaxation rate for a single NV near the silver increases with temperature (red circles in Fig. 3A), as expected for thermal noise, but the scaling is clearly nonlinear. This can be understood by recognizing that the conductivity of the silver film is also a function of temperature and that the magnitude of the thermal currents in the silver depends on the conductivity. To account for this effect, a four-point resistance measurement of the silver film is performed to determine the temperature dependence of the bulk conductivity of the silver film (Fig. 3B).

To analyze the dependence of the NV spin relaxation rate on distance, temperature, and conductivity, we use the model of (6), in which an electronic spin-1/2 qubit with Larmor frequency  $\omega_L$  is positioned at a distance  $d$  from the surface of a metal. For silver at room temperature,

the skin depth at  $\omega_L$  is  $\delta \approx 1$   $\mu$ m; consequently, when  $d < 100$  nm, we are in the “quasi-static” limit  $d \ll \delta$ . The thermal limit  $k_B T \gg \hbar\omega_L$  is valid for all temperatures in this work. In this regime, the magnetic noise spectral density perpendicular to the silver surface is given by

$$S_B^z = \frac{\mu_0^2}{16\pi} \frac{k_B T \sigma}{d} \quad (1)$$

where  $\sigma$  is the temperature-dependent conductivity of the metal as defined by the Drude model. This scaling can be intuitively understood by considering the magnetic field generated by a single thermal electron in the metal at the NV position,  $B_0 = \frac{\mu_0 e v_{\text{th}}}{4\pi d^2}$ , where the thermal velocity  $v_{\text{th}} \propto \sqrt{k_B T/m_e}$ ,  $m_e$  is the effective mass of electrons in silver, and  $e$  is the electron charge. In the limit  $d \ll \delta$ , screening can be safely ignored, and the NV experiences the magnetic field

spectrum arising from  $N$  independent electrons in a volume  $V$ ;  $S_B \propto V n \langle B_0 \rangle^2 \tau_c$ , where  $n$  is the electron density and  $\tau_c$  is the correlation time of the noise, given by the average time between electron scattering events; and  $\tau_c = l/v_F$ , where  $l$  is the electron mean free path and  $v_F$  is the Fermi velocity. Recognizing that the NV is sensitive to the motion of electrons within a sensing volume  $V \propto d^3$ , we arrive at the scaling given by Eq. 1, with  $\sigma = \frac{n e^2 \tau_c}{m_e}$ . Applying Fermi's golden rule and accounting for the orientation and spin-1 of the NV yields the relaxation rate for the  $|m_s = 0\rangle$  state

$$\Gamma = \frac{1}{T_1} = \frac{3g^2 \mu_B^2}{2h^2} S_B^z \left( 1 + \frac{1}{2} \sin^2(\theta) \right) \quad (2)$$

where  $g \approx 2$  is the electron g-factor,  $\mu_B$  is the Bohr magneton, and  $\theta \approx 54.7^\circ$  is the angle of the

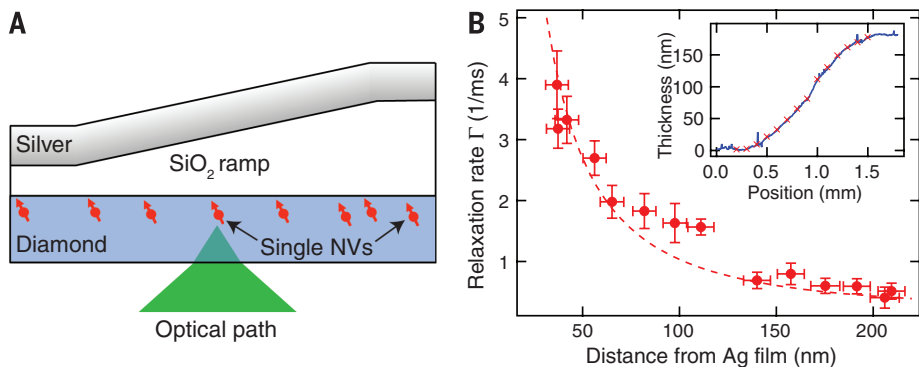


**Fig. 2. Distance dependence of NV relaxation close to silver.** (A) A gradual  $\text{SiO}_2$  ramp (slope of  $\sim 0.2$  nm/ $\mu$ m) is grown on the diamond surface, followed by a 60-nm silver film. (B) The NV relaxation rate is measured as a function of position along the ramp, which is then converted to distance to the film. At each point, 5 to 10 NV centers are measured, and the minimum rate measured is plotted (red circles). The horizontal error bars reflect 1 SD in the estimated distance to the film including the uncertainty in NV depth, while the vertical error bars reflect 1 SD in the fitted relaxation rate. The red dashed line shows the expected relaxation rate with no free parameters after accounting for the finite silver film thickness. (Inset) Thickness of the ramp as a function of lateral position along the diamond sample (blue curve). The red crosses correspond to the positions along the sample where the measurements were taken.

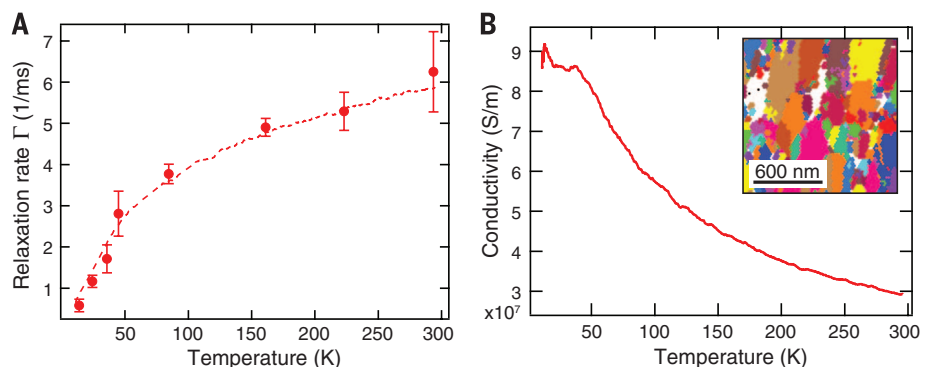


**Fig. 3. Temperature dependence of NV relaxation close to polycrystalline silver.** (A) The measured relaxation rate of a single NV spin under a polycrystalline silver film as a function of temperature (red data points). The error bars reflect 1 SD in the fitted relaxation rate. The conductivity of the silver film as a function of temperature shown in (B) is included in a fit to Eq. 2, with the distance to the film as the single free parameter (red dashed line). The extracted distance is  $31 \pm 1$  nm. (B) The conductivity of the 100-nm-thick polycrystalline silver film deposited on the diamond surface is measured as a function of temperature. (Inset) Grain boundaries within the polycrystalline silver film, imaged using electron backscatter diffraction. The average grain diameter is 140 nm, with a SD of 80 nm.

NV dipole relative to the surface normal vector (23). In Fig. 2B, the inverse scaling with distance  $d$  predicted by Eq. 1 is clearly evident for NVs very close to the silver. At distances comparable to the silver film thickness, Eq. 1 is no longer valid, but we recover excellent agreement with the no-free-parameters prediction of Eq. 2 by including a correction for the thickness of the silver film (red dashed line in Fig. 2B), which is measured independently. The measured relaxation rates as a function of temperature are also in excellent agreement with the predictions of Eq. 2 (red dashed line in Fig. 3A), while the extracted distance of  $31 \pm 1$  nm is consistent with the expected depth (23).

**Notably, very different results are obtained when we replace the polycrystalline film with single-crystal silver.** For this experiment, a 1.5- $\mu\text{m}$ -thick single-crystal silver film grown by sputtering onto silicon (23, 25, 26) is placed in contact with the diamond surface. The measured conductivity of the single-crystal silver exhibits a much stronger temperature dependence (blue line in Fig. 4A) as compared to that of the 100-nm-thick polycrystalline film. Figure 4B

presents the measured relaxation rate as a function of temperature for an NV in a region in direct contact with the single-crystal silver (blue squares). The dashed blue line corresponds to the temperature-dependent rate predicted by Eq. 2, which strongly disagrees with the experimental results. Specifically, because the measured silver conductivity increases faster than the temperature decreases in the range from room temperature down to 40 K, Eq. 2 predicts that the relaxation rate should increase as the temperature drops, peaking at 40 K and then dropping linearly with temperature once the conductivity saturates. Instead, the  $T_1$  of the NV consistently increases as the temperature drops, implying that at lower temperatures, the silver produces considerably less noise than expected from Eq. 2. We observe similar deviation from the prediction of Eq. 2 for all 23 NVs measured in the vicinity of the single-crystal silver (23).

To analyze these observations, we note that the conventional theoretical approach (6) resulting in Eq. 2 treats the motion of the electrons in the metal as entirely diffusive, using Ohm's law,

$J(\mathbf{r}, t) = \sigma \mathbf{E}(\mathbf{r}, t)$ , to associate the bulk conductivity of the metal with the magnitude of the thermal currents. While accurately describing the observed relaxation rates next to the polycrystalline material, where the resistivity of the film is dominated by electron scattering off grain boundaries (Fig. 3B, inset), this assumption is invalid in the single-crystal silver film experiments, particularly at low temperatures. Here, the measured conductivity of the single-crystal film indicates that the mean free path  $l$  is greater than 1  $\mu\text{m}$ , considerably exceeding the sensing region determined by the NV-metal separation, and thus the ballistic motion of the electrons must be accounted for. Qualitatively, the correlation time of the magnetic noise in this regime is determined by the ballistic time of flight of electrons through the relevant interaction region  $\tau_c \sim d/v_F$  (Fig. 4C). This results in a saturation of the noise spectral density and the spin relaxation rate  $\Gamma$  as either the NV approaches the silver surface or the mean free path becomes longer at lower temperatures (23), with the ultimate limit to the noise spectrum given by:

$$S_B^z = \frac{2 \mu_0^2 k_B T}{\pi} \frac{n e^2}{m_e v_F} \quad (3)$$

This regime of magnetic Johnson noise was recently analyzed theoretically (11) using the Lindhard form nonlocal dielectric function for the metal modified for finite electron scattering times (23, 27, 28). Comparison of this model (solid line in Fig. 4B) to the data, with distance again as the only free parameter, yields excellent agreement for all 23 measured NVs (23). Figure 4D shows the measured  $T_1$  times at 103 and 27 K for each NV as a function of extracted distance (blue triangles). Of the 23 NVs measured, 15 are in a region of the diamond sample in direct contact with the silver (23). Excellent agreement between the nonlocal model (solid lines) and the data is observed for all 23 NVs at all 12 measured temperatures. Apparent in Fig. 4D is the saturation of the relaxation rate as the NV approaches the silver surface and as the mean free path becomes longer at lower temperatures (dashed black line), as predicted by Eq. 3.

Although ballistic electron motion in nanoscale structures has previously been studied and utilized (12, 13), our approach allows for non-invasive probing of this and related phenomena and provides the possibility for studying mesoscopic physics in macroscopic samples. The combination of sensitivity and spatial resolution demonstrated here enables direct probing of current fluctuations in the proximity of individual impurities, with potential applications such as imaging of Kondo states and probing of novel two-dimensional materials (29), where our technique may allow for the spatially resolved probing of edge states (12). Likewise, it could enable investigation of the origin of  $1/f$  flux noise by probing magnetic fluctuations near superconducting Josephson circuits (30, 31). Finally, as Johnson noise presents an important limitation to the control of classical and quantum mechanical devices at small length scales (6–10), the present

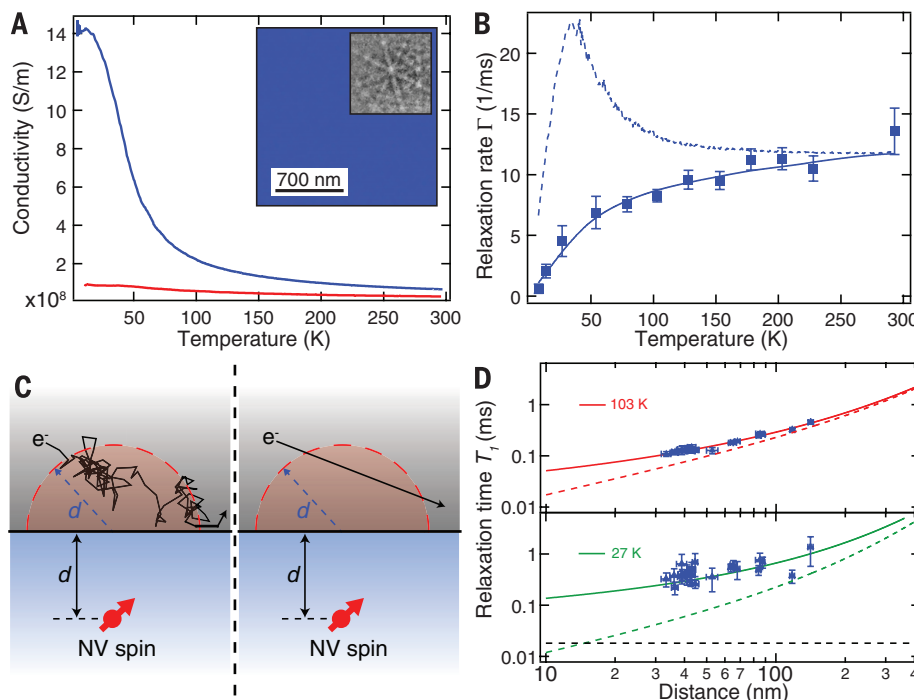


**Fig. 4. Temperature dependence of NV relaxation close to single-crystal silver.** (A) Measured conductivity of single-crystal (blue curve) and polycrystalline (red curve, same as Fig. 3B) silver as a function of temperature. (Inset) Electron backscatter diffraction image of the single-crystal silver film showing no grain boundaries, and the observed diffraction pattern. (B) Relaxation of a single NV spin under single-crystal silver as a function of temperature (blue squares). The error bars reflect 1 SD in the fitted relaxation rate. Equation 2 is fit to the data from 200 to 295 K (blue dashed line). A nonlocal model (23) is fit to the data (blue solid line); the extracted distance between the NV and the silver surface is  $36 \pm 1$  nm. (C) Cartoon illustrating the relevant limits, where the noise is dominated by diffusive electron motion (left,  $l \ll d$ ) and ballistic motion (right,  $l \gg d$ ). (D) The same data as in (B) were taken for 23 NVs at varying distances from the film. The  $T_1$  of each NV at 103 K (top) and 27 K (bottom) is plotted against the extracted depth (blue triangles). The horizontal error bars reflect 1 SD in the fitted distance to the film, while the vertical error bars reflect 1 SD in the fitted relaxation time. The nonlocal model (solid colored lines) saturates at a finite lifetime determined by Eq. 3 (bottom, dashed black line), whereas the local model does not (dashed colored lines).

results demonstrate that this limitation can be circumvented by operating below the length scale determined by the electron mean free path.

## REFERENCES AND NOTES

1. M. Lundstrom, *Science* **299**, 210–211 (2003).
2. B. Weber *et al.*, *Science* **335**, 64–67 (2012).
3. Q. Xu, B. Schmidt, S. Pradhan, M. Lipson, *Nature* **435**, 325–327 (2005).
4. L. Novotny, B. Hecht, *Principles of Nano-optics* (Cambridge Univ. Press, Cambridge, 2012).
5. A. L. Falk *et al.*, *Nat. Phys.* **5**, 475–479 (2009).
6. C. Henkel, S. Pötting, M. Wilkens, *Appl. Phys. B* **69**, 379–387 (1999).
7. Y. J. Lin, I. Teper, C. Chin, V. Vuletić, *Phys. Rev. Lett.* **92**, 050404 (2004).
8. M. P. A. Jones, C. J. Vale, D. Sahagun, B. V. Hall, E. A. Hinds, *Phys. Rev. Lett.* **91**, 080401 (2003).
9. D. Harber, J. McGuirk, J. Obrecht, E. Cornell, *J. Low Temp. Phys.* **133**, 229–238 (2003).
10. M. Brownnutt, M. Kumph, P. Rabl, R. Blatt, <http://arxiv.org/abs/1409.6572> (2014).
11. L. S. Langsjoen, A. Poudel, M. G. Vavilov, R. Joynt, *Phys. Rev. A* **86**, 010301 (2012).
12. C. Beenakker, H. van Houten, *Solid State Phys.* **44**, 1–228 (1991).
13. S. Datta, *Electronic Transport in Mesoscopic Systems* (Cambridge Univ. Press, Cambridge, 1997).
14. A. C. Bleszynski-Jayich *et al.*, *Science* **326**, 272–275 (2009).
15. H. Bluhm, N. C. Koshnick, J. A. Bert, M. E. Huber, K. A. Moler, *Phys. Rev. Lett.* **102**, 136802 (2009).
16. D. Rothfuss, A. Reiser, A. Fleischmann, C. Enss, *Appl. Phys. Lett.* **103**, 052605 (2013).
17. L. Childress *et al.*, *Science* **314**, 281–285 (2006).
18. J. R. Maze *et al.*, *Nature* **455**, 644–647 (2008).
19. G. Balasubramanian *et al.*, *Nature* **455**, 648–651 (2008).
20. J. P. Tetienne *et al.*, *Science* **344**, 1366–1369 (2014).
21. E. Schäfer-Nolte, L. Schlipf, M. Ternes, F. Reinhard, K. Kern, J. Wachtrup, <http://arxiv.org/abs/1406.0362> (2014).
22. M. Pelliccione, B. A. Myers, L. Pascal, A. Das, A. C. Bleszynski Jayich, <http://arxiv.org/abs/1409.2422> (2014).
23. Materials and methods are available as supporting material on *Science* Online.
24. T. H. Taminiau, J. Cramer, T. van der Sar, V. V. Dobrovitski, R. Hanson, *Nat. Nanotechnol.* **9**, 171–176 (2014).
25. A. A. Baski, H. Fuchs, *Surf. Sci.* **313**, 275–288 (1994).
26. J. H. Park *et al.*, *Adv. Mater.* **24**, 3988–3992 (2012).
27. G. W. Ford, W. Weber, *Phys. Rep.* **113**, 195–287 (1984).
28. N. W. Ashcroft, N. D. Mermin, *Solid State Physics* (Holt, Rinehart and Winston, New York, 1976).
29. P. Maher *et al.*, *Science* **345**, 61–64 (2014).
30. L. Faoro, L. B. Ioffe, *Phys. Rev. Lett.* **100**, 227005 (2008).
31. S. M. Anton *et al.*, *Phys. Rev. Lett.* **110**, 147002 (2013).

## ACKNOWLEDGMENTS

We thank E. Demler, A. Bleszynski Jayich, B. Myers, A. Yacoby, M. Vavilov, R. Joynt, A. Poudel, and L. Langsjoen for helpful discussions and insightful comments. Financial support was provided by the Center for Ultracold Atoms, the National Science Foundation (NSF), the Defense Advanced Research Projects Agency Quantum-Assisted Sensing and Readout program, the Air Force Office of Scientific Research Multidisciplinary University Research Initiative, and the Gordon and Betty Moore Foundation. S.K. and A.S. acknowledge financial support from the National Defense Science and Engineering Graduate fellowship, V.E.M. from the Society of Fellows of Harvard University, and S.K. from the NSF Graduate Research Fellowship. All fabrication and metrology were performed at the Center for Nanoscale Systems (CNS), a member of the National Nanotechnology Infrastructure Network, which is supported by the NSF under award no. ECS-0335765. The CNS is part of Harvard University.

## SUPPLEMENTARY MATERIALS

[www.sciencemag.org/content/347/6226/1129/suppl/DC1](http://www.sciencemag.org/content/347/6226/1129/suppl/DC1)  
Materials and Methods

Figs. S1 to S7

Tables S1 to S3

References (32–34)

4 December 2014; accepted 16 January 2015

Published online 29 January 2015;

10.1126/science.aaa4298

## REPELLENT MATERIALS

# Robust self-cleaning surfaces that function when exposed to either air or oil

Yao Lu,<sup>1</sup> Sanjayan Sathasivam,<sup>1</sup> Jinlong Song,<sup>2</sup> Colin R. Crick,<sup>3</sup> Claire J. Carmalt,<sup>1</sup> Ivan P. Parkin<sup>1\*</sup>

**Superhydrophobic self-cleaning surfaces are based on the surface micro/nanomorphologies; however, such surfaces are mechanically weak and stop functioning when exposed to oil. We have created an ethanol suspension of perfluorosilane-coated titanium dioxide nanoparticles that forms a paint that can be sprayed, dipped, or extruded onto both hard and soft materials to create a self-cleaning surface that functions even upon emersion in oil. Commercial adhesives were used to bond the paint to various substrates and promote robustness. These surfaces maintained their water repellency after finger-wipe, knife-scratch, and even 40 abrasion cycles with sandpaper. The formulations developed can be used on clothes, paper, glass, and steel for a myriad of self-cleaning applications.**

**A**rtificial self-cleaning surfaces work through extreme water repellence (superhydrophobicity) so that water forms near spherical shapes that roll on the surface; the rolling motion picks up and removes dirt, viruses, and bacteria (1–3). To achieve near spherical water droplets, the surfaces must be highly textured (rough) combined with extremely low water affinity (waxy) (4, 5). The big drawback of these artificial surfaces is that they are readily abraded (6–8), sometimes with little more than brushing with a tissue, and readily contaminated by oil (9–11). We report here a facile method for making superhydrophobic surfaces from both soft (cotton or paper) and hard (metal or glass) materials. The process uses dual-scale nanoparticles of titanium dioxide ( $\text{TiO}_2$ ) that are coated with perfluorooctyltriethoxysilane. We created an ethanol-based suspension that can be sprayed, dipped, or painted onto surfaces to create a resilient water-repellent surface. By combining the paint and adhesives, we created a superhydrophobic surface that showed resilience and maintained its performance after various types of damage, including finger-wipe, knife-scratch, and multiple abrasion cycles with sandpaper. This method can also be used for components that require self-cleaning and lubricating such as bearings and gears, to which superamphiphobic (repels oil and water) surfaces (9–11) are not applicable.

A paint was created by mixing two different size ranges of  $\text{TiO}_2$  nanoparticles (~60 to 200 nm and ~21 nm) in an ethanol solution containing perfluorooctyltriethoxysilane (12). Scanning electron microscopy (SEM) and transmission electron microscopy (TEM) of the constituent particles

of the paint (Fig. 1A) show the dual-scale nature of the  $\text{TiO}_2$  nanoparticles. X-ray photoelectron spectroscopy (XPS) (Fig. 1B) showed that the titanium dioxide particles were coated with perfluorooctyltriethoxysilane.

We used many different coating methods to create the water-repellent surfaces, including an artist's spray-gun to coat hard substrates such as glass and steel, dip-coating for cotton wool, and a syringe (movie S1) to extrude the paint onto filter paper. After allowing the ethanol to evaporate for ~180 s at room temperature, the treated areas of the substrates supported water as near spherical droplets, whereas the untreated parts were readily wetted (it required ~30 min for the ethanol to fully evaporate from cotton wool and filter paper at room temperature) (fig. S1). We used x-ray diffraction (XRD) (Fig. 1C) to analyze the coatings on hard and soft substrates. The diffraction peaks show the expected patterns for nanoscaled  $\text{TiO}_2$ .

On a surface that shows water repellence, water droplets tend to bounce instead of wetting the surface (13, 14). However, for soft substrates, extreme superhydrophobicity is required to achieve the bouncing phenomenon because the water droplets tend to be trapped onto the threads of the substrates (cotton wool) (15). Shown in fig. S2 are the water droplet tests on untreated glass, steel, cotton wool, and filter paper, which were readily wetted (the contact angle of the water droplets and the solid surfaces is defined as 0). Shown in Fig. 2 is the water bouncing process on dip-coated glass, steel, cotton wool, and filter paper surfaces. Water droplets completely leave the surface without wetting or even contaminating the surfaces (the water was dyed blue to aid visualization), indicating that the surfaces were superhydrophobic. In movie S2, we compare the water-affecting behavior between untreated and treated glass, steel, cotton wool, and filter paper, respectively. The effect of artificial rain on the treated surfaces is shown in movie S3; the drop sizes varied with random impact

<sup>1</sup>Department of Chemistry, University College London, 20 Gordon Street, London, WC1H 0AJ, UK. <sup>2</sup>Key Laboratory for Precision and Non-traditional Machining Technology of Ministry of Education, Dalian University of Technology, Dalian, 116024, People's Republic of China. <sup>3</sup>Department of Chemistry, Imperial College London, South Kensington Campus, London, SW7 2AZ, UK.

\*Corresponding author. E-mail: i.p.parkin@ucl.ac.uk

*This copy is for your personal, non-commercial use only.*

**If you wish to distribute this article to others**, you can order high-quality copies for your colleagues, clients, or customers by [clicking here](#).

**Permission to republish or repurpose articles or portions of articles** can be obtained by following the guidelines [here](#).

***The following resources related to this article are available online at [www.sciencemag.org](http://www.sciencemag.org) (this information is current as of March 9, 2015):***

**Updated information and services**, including high-resolution figures, can be found in the online version of this article at:

<http://www.sciencemag.org/content/347/6226/1129.full.html>

**Supporting Online Material** can be found at:

<http://www.sciencemag.org/content/suppl/2015/01/28/science.aaa4298.DC1.html>

A list of selected additional articles on the Science Web sites **related to this article** can be found at:

<http://www.sciencemag.org/content/347/6226/1129.full.html#related>

This article **cites 27 articles**, 6 of which can be accessed free:

<http://www.sciencemag.org/content/347/6226/1129.full.html#ref-list-1>

This article appears in the following **subject collections**:

Materials Science

[http://www.sciencemag.org/cgi/collection/mat\\_sci](http://www.sciencemag.org/cgi/collection/mat_sci)

## Supplementary Materials for

### **Probing Johnson noise and ballistic transport in normal metals with a single-spin qubit**

S. Kolkowitz, A. Safira, A. A. High, R. C. Devlin, S. Choi, Q. P. Unterreithmeier, D. Patterson, A. S. Zibrov, V. E. Manucharyan, H. Park,\* M. D. Lukin<sup>1</sup>\*

\*Corresponding author. E-mail: [lukin@physics.harvard.edu](mailto:lukin@physics.harvard.edu) (M.D.L.); [hongkun\\_park@harvard.edu](mailto:hongkun_park@harvard.edu) (H.P.)

Published 29 January 2015 on *Science* Express  
DOI: 10.1126/science.aaa4298

#### **This PDF file includes:**

Materials and Methods  
Figs. S1 to S7  
Tables S1 to S3  
References (32–34)

# 1 Experimental materials and methods

The experiments were performed using 30 micron thick electronic grade diamonds grown, thinned, and polished by Element Six with a natural isotopic abundance of carbon. Shallow NV centers were generated through Nitrogen-14 implantation at 6 keV energy at a density of  $2 \times 10^9/\text{cm}^2$ , followed by annealing at 800 °C. The single-crystal silver films were grown by sputtering at 300 °C onto a (111) oriented single-crystal silicon substrate [25, 26], with a deposition rate of  $\sim 1.5 \text{ nm/s}$ , as discussed in detail in section 2.1. The polycrystalline silver films were evaporated directly onto the diamond. A 5-nm layer of silica ( $\text{SiO}_2$ ) was grown on the diamond surface prior to the metal deposition to preserve NV properties. Temperature dependence measurements were performed in a Montana Instruments closed cycle cryostat.

## 1.1 Averaging, number of points, and wait times for relaxation measurements

All  $T_1$  measurements in this work are composed of the average of many repeated sequences as described in Figure 1B of the main text. Number of averages, number of points, and the range of evenly spaced wait times for each figure are given in Table SI. All error bars shown in this work correspond to one standard deviation.

# 2 Fabrication and metrology

## 2.1 Single-crystal silver deposition and characterization

The single-crystalline silver films were grown using direct current plasma sputtering (AJA International Orion 3) [25, 26]. The sputtering targets used were 99.99% pure silver (Kurt Lesker, Inc.). Films were deposited onto prime-grade, degenerately doped (111)-Si wafers (0.0015–0.005  $\Omega\text{-cm}$ ). The substrates were ultrasonically cleaned in acetone, followed by a 2:1 sulfuric acid:hydrogen peroxide solution to eliminate organics. The substrates were then immersed in 49% hydrofluoric acid for 10–15 seconds to remove any native oxide. Next, the substrates were rapidly transferred into the sputtering chamber and the chamber was pumped down to minimize re-oxidation of the surface. Upon reaching a base pressure of about  $5 \times 10^{-7}$  Torr, the substrate was heated to 300 °C and silver was deposited at a rate of 1.5–1.7 nm/s.

Following the growth, multiple characterization techniques were used to test the quality of the deposited films. The crystallinity and surface quality of the films were probed via transmission electron microscopy (TEM) and atomic force microscopy (see Figure SI). The TEM scans confirm that the silver films are single-crystal, with lattice fringes apparent from the bulk to the surface. The AFM scans confirm that the films are ultra-smooth with typical root-mean-square roughness of  $\sim 1 \text{ nm}$ . Consistent with the TEM scans and electron backscatter diffraction imaging (see below), no grain boundaries were observed within the  $10 \mu\text{m} \times 10 \mu\text{m}$  scan region.

## 2.2 Characterization of silver film grain size

Crystal orientation and average grain size of the silver samples were measured with electron backscatter diffraction (EBSD). For the polycrystalline films, we use as reference a 100 nm film deposited on 5 nm of  $\text{SiO}_2$  on (100) silicon. In the insets of Figures 3 and 4 of the main text, inverse pole figures of the electron backscatter diffraction data were post-processed to highlight grain boundaries. The areas in white are areas of large noise where the the crystal orientation could not be discerned with high confidence, while the other colors indicate different crystal orientations. The inverse pole figures from which those images are derived are given in Figure S2. EBSD data of the polycrystalline silver film indicated a very granular film, with an average grain diameter of 140 nm and a standard deviation of 80 nm. Grain diameter was approximated by taking the diameter of the circle with the same area as each grain. For the single-crystal films, EBSD data indicated the sample is a single-crystal from nanometer to millimeter length scales, and confirmed a (111) exposed crystal surface for the single-crystal silver, as expected from the growth conditions.

## 2.3 Diamond surface characterization

AFM and profilometer scans were performed on the implantation-side surface of the diamond used for the single-crystal silver measurements, as shown in Figure S3. The diamond was found to have a local surface roughness of  $\sim 1 \text{ nm RMS}$  over a  $10 \mu\text{m} \times 10 \mu\text{m}$  range, and to have variations of  $\sim 10\text{-}20 \text{ nm peak to peak}$  at the  $\sim 100 \text{ micron}$  length scale across the entire sample. The NVs sampled from the spatial region over which the diamond was considered to be in contact with the silver were all within a single  $40 \mu\text{m} \times 40 \mu\text{m}$  field of view (see subsection 5.2 for details.)

## 2.4 Spacer layer fabrication for distance dependance studies

Distance-dependence studies of the noise were carried out by growing a spacer layer of  $\text{SiO}_2$  between the evaporated silver metal and diamond. A 5-nm thick film of  $\text{SiO}_2$  was first deposited via CVD on the diamond. A  $100 \mu\text{m}$  thick sapphire slide was then placed  $\sim 300 \mu\text{m}$  above the surface of a diamond crystal-bonded to a silicon carrier wafer (see illustration in Figure S4.) The anisotropic CVD  $\text{SiO}_2$  deposition results in a smooth ramp, as measured by a profilometer (See Figure 2 of the main text). A 60 nm film of silver was then deposited on the structure in an electron-beam evaporator.

## 2.5 Fabrication of devices for temperature-dependent studies

For the temperature dependence measurements under evaporated polycrystalline silver (Fig. 3 in the main text), a 5 nm layer of silica was deposited onto the diamond via CVD growth, and a 100 nm layer of silver was then deposited onto the silica film.

In the case of the measurements under single-crystal silver, direct-deposition techniques to create single-crystal silver directly on diamond devices do not presently exist. Instead, the device used in this experiment was fabricated using optical contact bonding between the diamond and the single-crystal silver surfaces. The diamond sample was prepared for bonding by cleaning in a boiling 1:1:1 solution of nitric, sulfuric, and perchloric acids for at least one hour, directly prior to bonding. After growth, the single-crystal silver films were stored with a 50 nm capping layer of alumina to prevent surface oxidation. Directly prior to the bonding process, the alumina capping layer was stripped away in hydrofluoric acid. The diamond was then placed NV side down in contact with the freshly exposed silver surface. A drop of de-ionized water was placed on top of the diamond and allowed to wick in-between the diamond and the silver, and the diamond was lightly pressed against the silver from above, while the two samples were blow-dried with a nitrogen spray gun, leaving the diamond bonded directly to the silver surface. This procedure was performed in a cleanroom, with careful attention to the cleanliness of the tweezers and sample holders. Several attempts were required to produce the final device used in this experiment, which demonstrated very robust bonding between the diamond and the silver, and survived multiple thermal cycles from 300-10 K.

### 3 Johnson Noise Theory

#### 3.1 Spin decay rate near a conducting metallic half-space

We derive expressions for the lifetime of a spin interacting with magnetic Johnson noise above a metallic half space following the prescriptions of [6] and [11].

From Fermi's golden rule and the fluctuation-dissipation theorem, the decay rate from  $|m_s = 0\rangle$  to  $|m_s = 1\rangle$  for a spin-1 system at a distance  $z$  above the surface of a metal at temperature  $T$ , with level separation  $\omega$  and magnetic dipole moment in the  $i$ th direction is then given by

$$\Gamma_{0 \rightarrow 1} = \frac{\mu^2}{\hbar^2} \coth \left( \frac{\hbar\omega}{2k_B T} \right) S_B^{ii}(z, \omega) \quad (\text{S1})$$

where

$$S_B^x(z, \omega) = S_B^y(z, \omega) = \frac{\hbar}{8\pi\epsilon_0 c^3} \text{Re} \int_0^\infty dp \frac{p(\omega^2 r^p(p) + (p^2 c^2 - \omega^2) r^s(p))}{\sqrt{\omega^2 - p^2 c^2}} e^{2iz\sqrt{\omega^2/c^2 - p^2}} \quad (\text{S2})$$

$$S_B^z(z, \omega) = \frac{\hbar}{4\pi\epsilon_0 c^2} \text{Re} \int_0^\infty dp \frac{p^3}{\sqrt{\omega^2/c^2 - p^2}} e^{2iz\sqrt{\omega^2/c^2 - p^2}} r^s(p), \quad (\text{S3})$$

and  $r^p$  and  $r^s$  denote the Fresnel Coefficients for plane waves incident on the material interface for  $p$  and  $s$  polarized light, respectively. We choose a coordinate system in which the  $z$  axis is perpendicular to the material interface; as  $S_B^{\alpha\beta}$  is a diagonal tensor in this coordinate system, we drop one index and denote the diagonal elements by identifying  $S_B^{ii} = S_B^i$ . We have also

assumed off-diagonal density matrix elements to be 0,  $\rho_{ij} = \langle i|\rho|j\rangle = \sum \delta_{ij}$ , consistent with  $T_2^*$  of the NVs in our experiment being much faster than the population dynamics of system.

### 3.2 Reflection coefficients

Explicitly, the reflection coefficients for a single material boundary are given by

$$r^s(p) = \frac{k_1 - k_2}{k_1 + k_2} \quad (S4)$$

$$r^p(p) = \frac{\epsilon_2 k_1 - \epsilon_1 k_2}{\epsilon_2 k_1 + \epsilon_1 k_2} \quad (S5)$$

with

$$k_1 = \sqrt{\epsilon_1 \omega^2 / c^2 - p^2} \quad (S6)$$

$$k_2 = \sqrt{\epsilon_2 \omega^2 / c^2 - p^2} \quad (S7)$$

where we have assumed  $\mu_i \approx 1$  in all space, consistent with the materials used in this study. In the case of a spin above a metal, the above coefficients are valid when the thickness of the metal greatly exceeds the skin depth or when the spin-metal distance is much less than the thickness. To take into account the finite thickness of the film, the reflection coefficients take the form

$$r^s(p) = \frac{k_1^2 - k_2^2}{k_1^2 + k_2^2 + 2ik_1 k_2 \cot(k_2 a)} \quad (S8)$$

$$r^p(p) = \frac{\epsilon_2 k_1 - \epsilon_1 k_2}{\epsilon_2 k_1 + \epsilon_1 k_2 + 2i\epsilon_2 k_1 k_2 \cot(k_2 a)}, \quad (S9)$$

where  $a$  is the thickness of the film [32].

In our experiments with polycrystalline silver, finite thickness effects have a significant impact on the noise power spectrum outside of the film. The distance and temperature dependence experiments, depicted in Figures 2 and 3 in the main text, used films with thicknesses  $a = 60$  nm and  $a = 100$  nm, respectively. The theoretical predictions shown in those figures incorporate these finite-thickness corrections. Conversely, in the case of the single-crystal films, which are much thicker ( $a = 1.5$   $\mu$ m), we find that the corrections due to finite thickness are negligible.

Furthermore, in the experiments involving polycrystalline silver, an extra 5 nm layer of  $\text{SiO}_2$  lies between the diamond and the metal. Such a geometry can also be accounted for with the appropriate reflection coefficients. However, because  $\mu \approx 1$  in diamond and  $\text{SiO}_2$ , the length scales  $z$  and electromagnetic field wave vectors  $|\mathbf{k}| = \epsilon\omega/c$  such that  $|\mathbf{k}|z \gg 1$ , and the electromagnetic response is dominated by  $|\epsilon_2| = |\epsilon_{\text{Ag}}| \gg \{|\epsilon_{\text{Diamond}}|, |\epsilon_{\text{SiO}_2}|, |\epsilon_{\text{SiO}_2}|, |\epsilon_{\text{Diamond}}|\}$ , the effects of the diamond medium and the silica layer are both negligible.

### 3.3 Quasi-static approximation

It is convenient to perform approximations to the integrals in equations (S2) and (S3) to gain insight into the decay rate behavior in different regimes. In particular, in the case of a full metallic half space, and in the regime where the electromagnetic wavelength is much larger than the skin depth of the metal,  $\lambda \gg \delta$ , and the skin depth is much larger than the spin's distance to the metal,  $\delta \gg z$ ,

$$S_B^x(z) = S_B^y(z) \approx \frac{\hbar\omega\sigma}{64\pi\epsilon_0^2 z} \quad (\text{S10})$$

$$S_B^z(z) \approx 2S_B^x \quad (\text{S11})$$

In this regime, known as the quasi-static regime, the decay rate, as described in equation (S1), is proportional to  $1/z$ , and thus  $T_1 = 1/\Gamma \propto z$ .

### 3.4 NV magnetic dipole orientation

We also must account for the orientation of the magnetic dipole of our NV centers when calculating the expected decay rate. The decay rate from  $|m_s = 0\rangle$  to  $|m_s = 1\rangle$  for a spin-1 system with a quantization axis making an angle  $\theta$  with  $\hat{z}$ , the vector normal to the metal surface, in the quasi-static limit is given by

$$\gamma_{0 \rightarrow 1} = \frac{1}{\hbar^2} \coth\left(\frac{\hbar\omega}{2k_B T}\right) \sum g^2 \mu_B^2 |\langle 1 | S_i | 0 \rangle|^2 S_B^i(z, \omega) \quad (\text{S12})$$

$$\approx \frac{g^2 \mu_B^2}{\hbar^2} \frac{2k_B T}{\hbar\omega} \left( \frac{1}{2} \cos^2(\theta) S_B^x(z, \omega) + \frac{1}{2} S_B^y(z, \omega) + \frac{1}{2} \sin^2(\theta) S_B^z(z, \omega) \right) \quad (\text{S13})$$

$$\approx \frac{g^2 \mu_B^2 \mu_0^2 k_B T \sigma}{32\pi z \hbar^2} \left( 1 + \frac{1}{2} \sin^2(\theta) \right). \quad (\text{S14})$$

where in our temperature and frequency range of interest ( $T > 4$  K and  $\omega < 20$  GHz),  $\coth(\hbar\omega/2k_B T) \approx 2k_B T/\hbar\omega$ , and we choose our coordinate system such that the spin is always in the  $x - z$  plane. All diamond samples used in the experiment are cut such that all four possible NV dipole orientations make the same angle  $\theta = \frac{1}{2}(180^\circ - \cos^{-1}(1/3)) \approx 54.7^\circ$  with  $\hat{z}$ .

### 3.5 Three-level system dynamics

We also must account for the population dynamics of our three level spin-1 coupled to a magnetic noise bath. The rate equations for this system are given by

$$\partial_t \begin{pmatrix} \rho_{00} \\ \rho_{-1-1} \\ \rho_{11} \end{pmatrix} = \begin{pmatrix} -2\gamma & \gamma & \gamma \\ \gamma & -\gamma & 0 \\ \gamma & 0 & -\gamma \end{pmatrix} \begin{pmatrix} \rho_{00} \\ \rho_{-1-1} \\ \rho_{11} \end{pmatrix}, \quad (\text{S15})$$

which, for boundary conditions  $\rho_{00}(t = 0) = 1$ , give the solution

$$\rho_{00}(t) = \frac{2}{3} \exp(-3\gamma t) + \frac{1}{3}. \quad (\text{S16})$$

Thus, the population decay from the  $m_s = 0$  state is a factor 3 larger than the rate given by equation (S14), and we arrive at

$$\Gamma \approx \frac{3\mu^2 g^2 \mu_B^2 k_B T \sigma}{32\pi \hbar^2 z} \left( 1 + \frac{1}{2} \sin^2 \theta \right), \quad (\text{S17})$$

which is equivalent to equation (2) given in the main text.

### 3.6 Non-local corrections to the decay rate

To take into account the ballistic nature of the electron motion in the silver, we follow [11] and introduce a non-local permittivity. In this regime we find  $S_B^z \approx 2S_B^x$  still holds, so for simplicity in the discussion that follows we consider only  $S_B^z$ . With the Lindhard form modified for finite electron lifetime, the  $s$  polarized reflection coefficient becomes

$$r^s(k_x, k_y) = \frac{\frac{2iqc^2}{\pi\omega^2} \int_0^\infty \frac{d\kappa}{\epsilon_t(k, \omega) - c^2 k^2/\omega^2} - 1}{\frac{2iqc^2}{\pi\omega^2} \int_0^\infty \frac{d\kappa}{\epsilon_t(k, \omega) - c^2 k^2/\omega^2} + 1}, \quad (\text{S18})$$

with  $k^2 = p^2 + \kappa^2$  and the transverse permittivity defined as

$$\epsilon_t(k, \omega) = 1 - \frac{\omega_p^2}{\omega(\omega + i\nu)} f_t((\omega + i\nu)/kv_f), \quad (\text{S19})$$

and the function  $f_t$  defined as

$$f_t(x) = \frac{3}{2}x^2 - \frac{3}{4}x(x^2 - 1) \ln \left( \frac{x+1}{x-1} \right), \quad (\text{S20})$$

and  $\omega_p$  is the electron plasma frequency,  $\nu$  is the electron scattering rate,  $\omega$  is the frequency of radiation, and  $v_f$  is the Fermi velocity. In the above expressions, the non-locality manifests itself through the  $k$  dependence of the permittivity. In order to derive an analytical expression for  $S_B^z$  in the limit  $z \rightarrow 0$ , we first rewrite the  $S_B^z$  in terms of the rescaled, dimensionless momentum  $\tilde{p} = (v_f/\nu)p$  and introduce  $\alpha = \frac{\nu}{\omega} \frac{c}{v_f}$ :

$$S_B^z = \frac{\hbar}{4\pi\epsilon_0 c^2} \frac{\nu^3}{v_f^3} \text{Re} \int_0^\infty d\tilde{p} \frac{\tilde{p}^3}{\sqrt{1/\alpha^2 - \tilde{p}^2}} e^{i\frac{2\nu z}{v_f} \sqrt{1/\alpha^2 - \tilde{p}^2}} r^s(\tilde{p}) \quad (\text{S21})$$

$$r^s(\tilde{p}) = \frac{2i\sqrt{1/\alpha^2 - \tilde{p}^2} \int_0^\infty \frac{d\kappa}{\epsilon_t/\alpha^2 - \tilde{p}^2 - \kappa^2} - \pi}{2i\sqrt{1/\alpha^2 - \tilde{p}^2} \int_0^\infty \frac{d\kappa}{\epsilon_t/\alpha^2 - \tilde{p}^2 - \kappa^2} + \pi}. \quad (\text{S22})$$

In the regime of our interest  $\alpha \sim 10^6$ , we can replace  $\sqrt{1/\alpha^2 - \tilde{p}^2}$  with  $i\tilde{p}$  to good approximation. Also, by separating the real and imaginary parts of the numerator and the denominator of equation (S22), it can be shown that when  $\nu/\omega \sim 10^3 \gg 1$ , the imaginary part of  $r^s$  is well-approximated by

$$\text{Im}(r^s) \approx \frac{\tilde{p}}{\pi \alpha^2} \int_0^\infty \frac{\text{Im}(\epsilon_t) d\tilde{\kappa}}{(\tilde{p}^2 + \tilde{\kappa}^2)^2}. \quad (\text{S23})$$

Finally, the substitution of equation (S23) into equation (S21) and the change of variables  $\tilde{p} = r \cos(\theta)$ , and  $\tilde{\kappa} = r \sin(\theta)$ , and  $\tan(\phi) = 1/r$  give us

$$S_B^z = \frac{\hbar}{4\pi^2 \epsilon_0 c^4} \frac{\omega_p^2 \omega}{v_f} C(2\nu z/v_f) \quad (\text{S24})$$

where the dimensionless function  $C(a)$  is given by

$$C(a) = \int_0^{\pi/2} \int_0^{\pi/2} d\theta d\phi \frac{\cos^3(\theta) e^{-a \frac{\cos(\theta)}{\tan(\phi)}}}{\sin(\phi) \cos^2(\phi)} \frac{3}{2} \left( \frac{\pi/2 - \phi}{\cos(\phi)} - \sin(\phi) \right). \quad (\text{S25})$$

The function  $C(a)$  has a logarithmic divergence  $C(a) \approx -\frac{\pi}{2} \ln(a)$  in the limit  $a \rightarrow 0$ . This originates from integration over infinitely large momentum  $p$  in the integral in equation (S3). Therefore, we introduce a physical cut-off, which modifies the range of integration for  $\phi$  from  $[0, \pi/2]$  to  $[\phi_c, \pi/2]$  with  $\tan(\phi_c) \equiv \frac{\nu}{v_f k_{\text{cut}}}$ . Using  $k_{\text{cut}} = 2\pi/a_{\text{Ag}}$  with  $a_{\text{Ag}} = 0.4$  nm, the lattice spacing of silver, we obtain well-defined behavior in the limit  $z \rightarrow 0$ ,  $C_{\text{cut}}(2\nu z/v_f) \approx 4.6\pi$ , which leads to Eq. 3 in the main text.

## 4 Spectral dependance of Johnson noise

From equation (S17), it is clear that we expect the noise spectrum of magnetic Johnson noise to be white for frequencies over which  $\coth(\hbar\omega/2k_B T) \approx 2k_B T/\hbar\omega$ . We verify this by applying an external magnetic field,  $B_{\parallel}$ , along the NV axis to tune the NV spin transition frequencies

$$\omega_{\pm} = \Delta \pm 2g\mu_B B_{\parallel}/\hbar \quad (\text{S26})$$

where  $\omega_{\pm}$  denotes the transition frequency from the  $|m_s = 0\rangle$  to the  $|m_s = \pm 1\rangle$  states,  $\Delta$  denotes the NV spin ground state zero-field splitting ( $2\pi \times 2.88$  GHz), and  $g\mu_B$  is the NV electronic spin magnetic moment. We measure the relaxation rate when the NV is initially polarized in the  $|0\rangle$  state, and when it is initially polarized in the  $|\pm 1\rangle$  states. Based on the rate equations given in section 1.2 (equation (S15)), the population relaxation from the  $|0\rangle$  state is given by equation (S16), while the population relaxation from the  $|\pm 1\rangle$  state takes the following form:

$$\rho_{\pm 1 \pm 1}(t) = \frac{1}{6}e^{-3\gamma t} + \frac{1}{2}e^{-\gamma t} + \frac{1}{3}. \quad (\text{S27})$$

We observe excellent agreement with these predictions, and simultaneously fit to the relaxation from the  $|0\rangle$  and  $|\pm 1\rangle$  states with only a single decay rate  $\gamma$ . A representative data set and fit are shown in Fig. 1D of the main text. The extracted rates  $\gamma$  at different magnetic fields, and therefore different NV transition frequencies, are shown in Figure S5. We find good agreement with the hypothesis of a white noise bath, with  $\chi^2/N = .87$ , for the  $\omega = 2\pi \times 2.2 - 3.6$  GHz range.

## 5 NV $T_1$ statistics

For NVs implanted at shallow depth such as the ones used in this work, we occasionally observe short NV  $T_1$  times for NVs under bare diamond (see Table SII). The origin of the fast decay is unclear. No spatial correlations in  $T_1$  are observed for the NVs with reduced  $T_1$  times.

### 5.1 Extraction of relaxation rates and distances under polycrystalline silver

As we would expect due to the variability in NV  $T_1$  times under bare diamond, when measuring under silver we observe a spread in the  $T_1$  times of the NVs, as shown in Figure S6, especially at larger distances from the silver, consistent with the variation we observe on bare diamond. This is because the Johnson noise only sets an upper limit on the NV spin lifetime, and other local sources of noise can still reduce it further. To compensate for this we measured 5-10 NVs at each point along the ramp, such that we can expect the maximum  $T_1$  observed in at each point to be Johnson noise limited (10 NVs per points were measured for the 7 closest points measured from 20-80 nm, and 5 NVs per points for the other 7 points, from 100-200 nm). We then only include NVs with a spin-dependent fluorescence contrast within the expected range of 15-35%. The result is plotted in Figure S6. The data plotted in Figure 2 in the main text is the inverse of the maximum  $T_1$  measured at each point along the ramp (the red data points in Figure S6).

In the theoretical prediction for the distance-dependent relaxation rate shown in Figure 2 of the main text, we include a correction to the lifetime predicted by equation (S1) to account for the phonon-induced NV spin relaxation at room temperature,  $T_1^{\text{ph}} = 6$  ms, consistent with our measured  $T_1$  times under bare diamond and previous studies [33]. This is a significant correction only at larger distances from the film and only at room temperature [33], and has a negligible impact on the measurements and analysis presented in all other figures.

When estimating the distance to the film for the NVs plotted in Figure 2 in the main text, the largest source of error is the variation in depth below the surface of the implanted NVs. As a result, we must also account for the statistical bias in NV depth introduced by selecting the maximum  $T_1$  in each region. In particular, as most NVs have Johnson noise limited lifetimes,

by taking the maximum  $T_1$  measured we are likely selecting not only for an NV with a  $T_1$  limited by Johnson noise, but also for the deepest NV in each region. To account for this, we assume the NV implantation depths are normally distributed, with a mean depth  $\mu=15$  nm and a standard deviation  $\sigma=10$  nm [34]. Let  $N_{\mu,\sigma}(x)$  denote the normal distribution representing the NV depth profile. If  $n$  NVs are randomly selected from this distribution, it can be shown that the probability the deepest NV selected has depth  $x$  is given by

$$P_{max}(x) = n \left( \int_{-\infty}^x N_{\mu,\sigma}(x') dx' \right)^{n-1} N_{\mu,\sigma}(x). \quad (\text{S28})$$

We use this new distribution to determine the expected value and standard deviation of the depth of the NV selected at each point along the ramp. For example, if we measured  $n = 5$  NVs at one point along the ramp, from the above probability distribution function  $P_{max}$  we find that the expected value for the depth of the deepest NV measured is 27 nm with a standard deviation of 7 nm, while at a point where we measured  $n = 10$  NVs the likely distribution of depths is  $30 \pm 6$  nm. These depths are then added to thickness of the ramp at that point to give the total distance to the silver surface plotted in Figure 2 of the main text.

In the temperature-dependence measurements shown in Figure 3A, an NV-film distance of  $d = 31 \pm 1$  nm is extracted from the fit to equation (2) in the main text. This is consistent with our expectations, as we expect a depth  $15 \pm 10$  nm from implantation parameters, in addition to the 5-nm thick  $\text{SiO}_2$  spacer layer.

## 5.2 NVs under single-crystal silver

In total, we measured the  $T_1$  of 25 NVs close to the single-crystal silver sample at 12 temperatures, in three different spatial regions on the sample. Each region was  $40 \mu\text{m} \times 40 \mu\text{m}$  in size, and the regions were each spatially separated from each other by more than  $100 \mu\text{m}$ . Of the 25 measured NVs, 16 were in region A (blue triangles in Figure S7D), where the diamond surface was observed to be in contact with the silver, 7 were in region B where a gap was expected to be growing between the diamond and the silver (pink squares in Figure S7D), and 2 were in region C, where the gap was expected to be fairly large (gray circles in Figure S7D).

The gap between the diamond and silver was qualitatively apparent based on a number of separate observations. We observed a variation in the brightness of the NVs in the different regions when exposed to the same laser power at the objective, which we attribute primarily to optical interference coming from the reflections off the silver and diamond surfaces. In addition, we measured reduced NV optical excited state lifetimes in region A (the region in contact with silver,) which we attribute to quenching from the silver (see Table SIII). We also observed an accumulation of a small amount of fluorescent background on the diamond surface over time in regions B and C, which was absent from region A, as would be expected if the diamond and silver were in direct contact there.

The  $T_1$  time at room temperature of all 25 NVs was also subsequently measured after the silver sample was removed. Of these NVs, one NV in region A was rejected because the measured

$T_1$  times under silver were not repeatable, and one NV in region B was rejected because it had very short  $T_1$  times even at low temperatures ( $<300 \mu\text{s}$  at 8 K,) leaving 23 NVs that compose the dataset shown in Figure 4D of the main text and Figure S7D). The anomalous behavior of the two rejected NVs is not well understood, and could be the subject of further study.

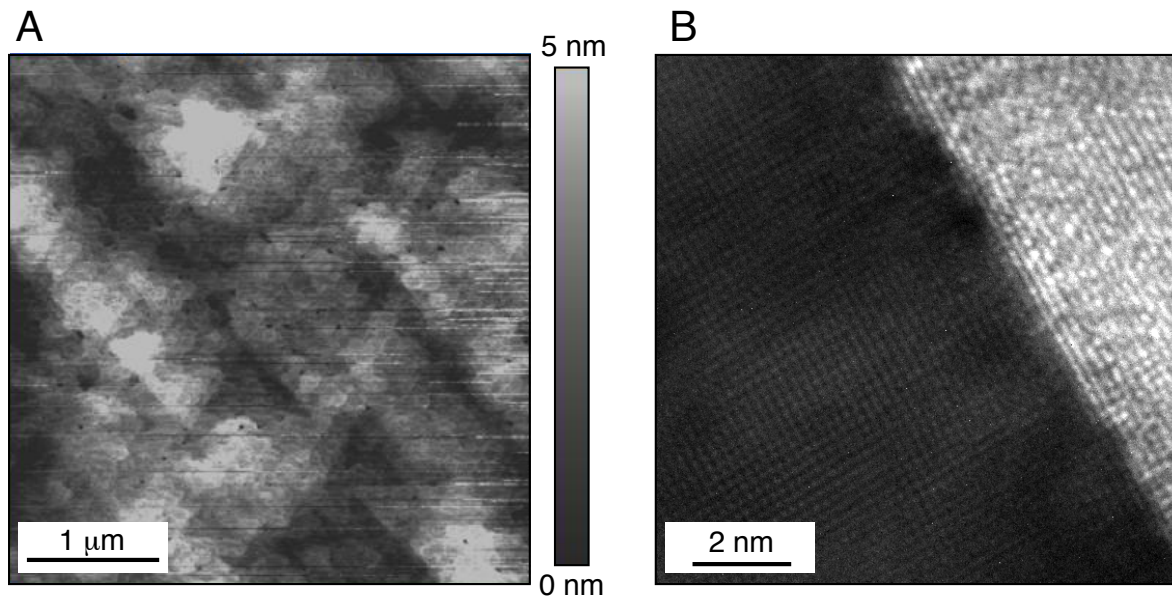
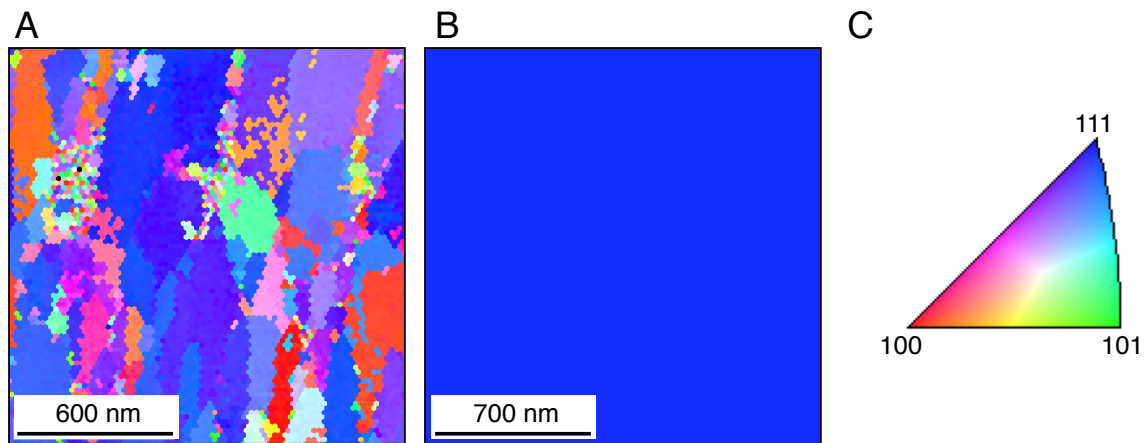


Figure S1: Single-crystal AFM and TEM characterization. **(A)** AFM image of a typical single-crystal silver surface grown for this work. The scan indicates a  $\sim 1$  nm RMS roughness over a  $4 \mu\text{m} \times 4 \mu\text{m}$  range, thus allowing for good diamond-silver contact. **(B)** A TEM image of a typical silver sample, where the growth direction is from left to right and the silver is capped with a titanium capping layer resulting in the brighter region on the right of the image. The image reveals single-crystallinity of the silver up to the surface.



**Figure S2: Single-crystal and polycrystalline silver Inverse Pole Figures (IPF).** Using electron backscatter diffraction imaging in an SEM, we image the local crystal orientations of our silver films, and measure the average grain size. **(A)** Data for a  $2 \mu\text{m} \times 2 \mu\text{m}$  area of evaporated silver on 5 nm of  $\text{SiO}_2$  on (100) silicon. The crystal variations along the direction perpendicular to the sample can cause mixed diffraction signals, and the crystal orientation fits in those regions have low confidence and result in an IPF with unphysical pixel-to-pixel variations in the crystal orientation (left region of image). **(B)** EBSD data for the same size region for single-crystal silver. No grain boundaries are visible. **(C)** Color scale conversion legend to map color to silver crystal orientation.

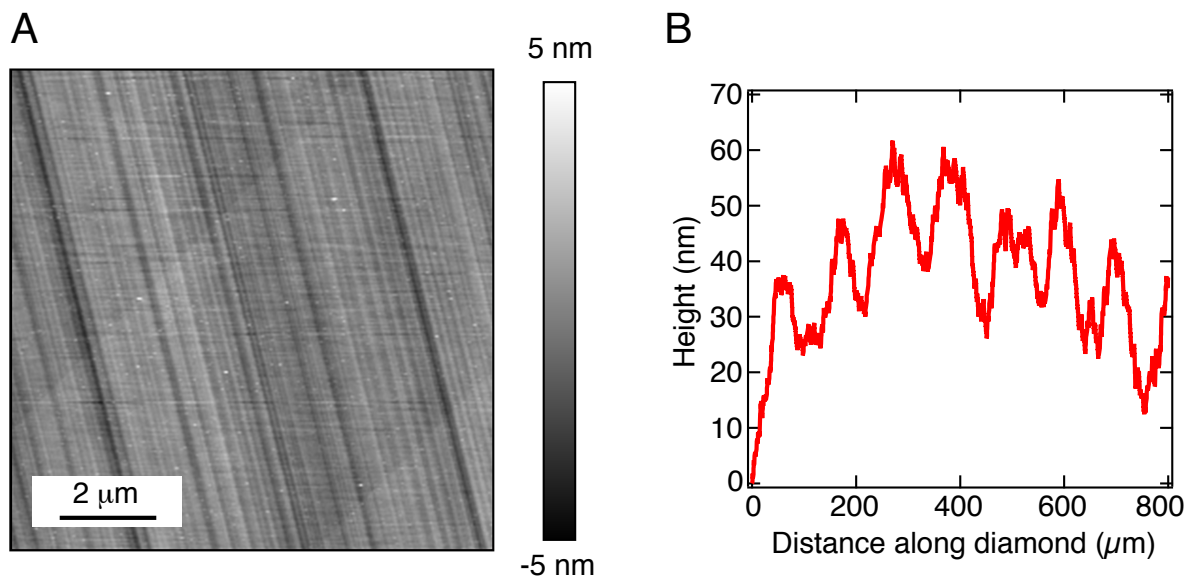
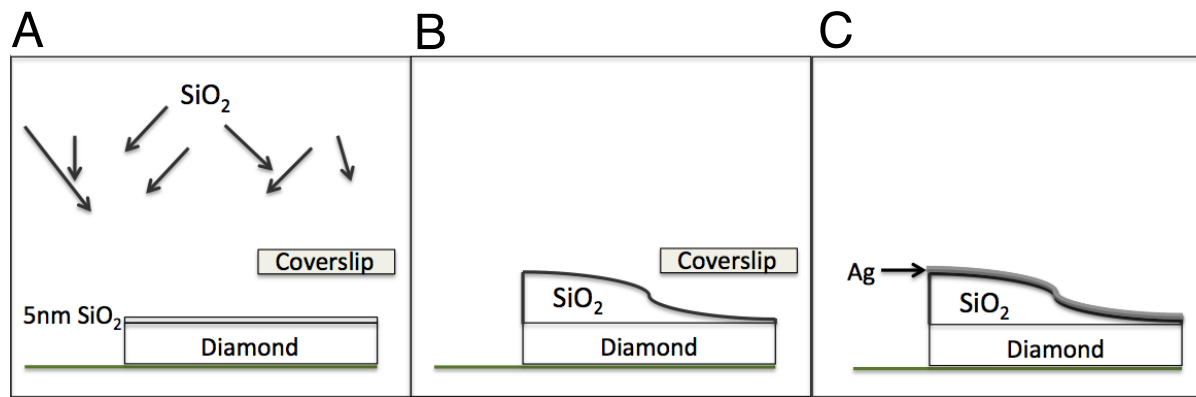


Figure S3: AFM and profilometer characterization of diamond surface. **(A)** An AFM image of the surface of the diamond used for the single-crystal silver measurements. The scan indicates a  $\sim 1$  nm RMS roughness over a  $10 \mu\text{m} \times 10 \mu\text{m}$  range, thus allowing for good diamond-silver contact. **(B)** A profilometer scan of the surface of the diamond sample.



**Figure S4: Silica ramp fabrication procedure.** (A,B) Following a 5 nm uniform CVD pre-deposition of SiO<sub>2</sub>, a silica layer of gradually increasing thickness is fabricated on a diamond sample by placing a raised coverslip (raised  $\sim 300 \mu\text{m}$ ) over the diamond, and growing the silica layer via an anisotropic CVD process. (C) A final 60 nm layer of silver is deposited on the ramp, so that NV centers at different points along the diamond are different distances away from the silver film.

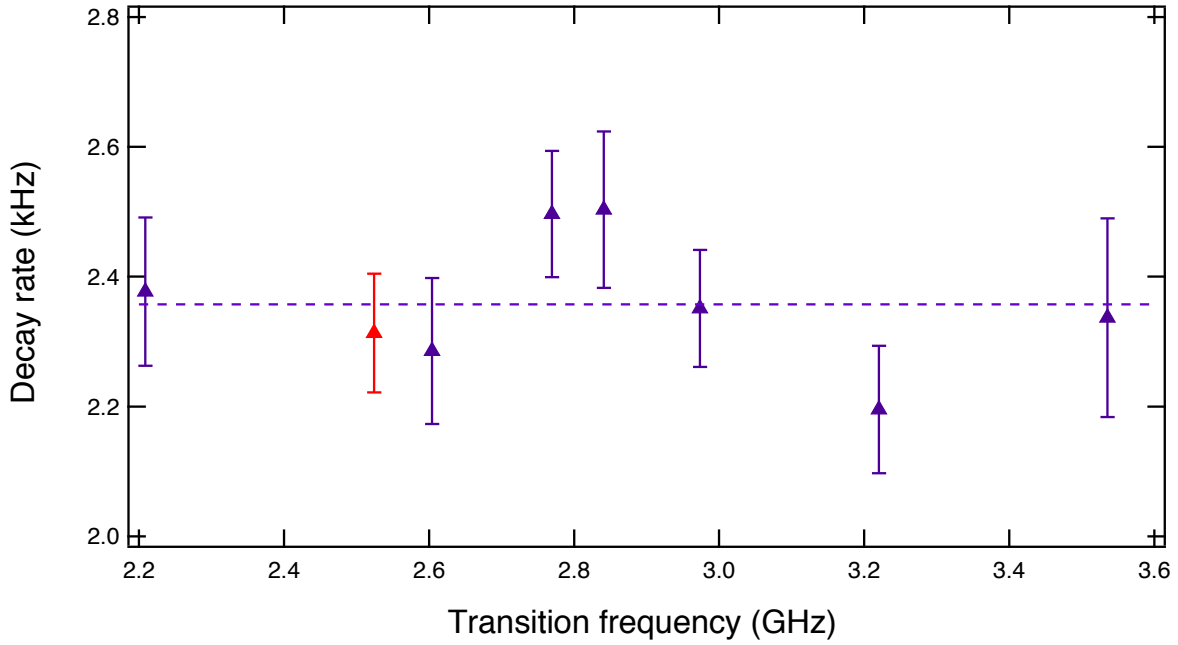


Figure S5: Johnson noise spectral dependence. We apply static magnetic fields to shift the NV spin transition frequencies. When polarized in the  $|\pm 1\rangle$  state, the relaxation rate of the NV center is sensitive to the magnetic field noise at the frequency  $\omega_{\pm}$  given by Eq. S26. The red triangle corresponds to the decay rate extracted from the data shown in Fig. 1D of the main text.

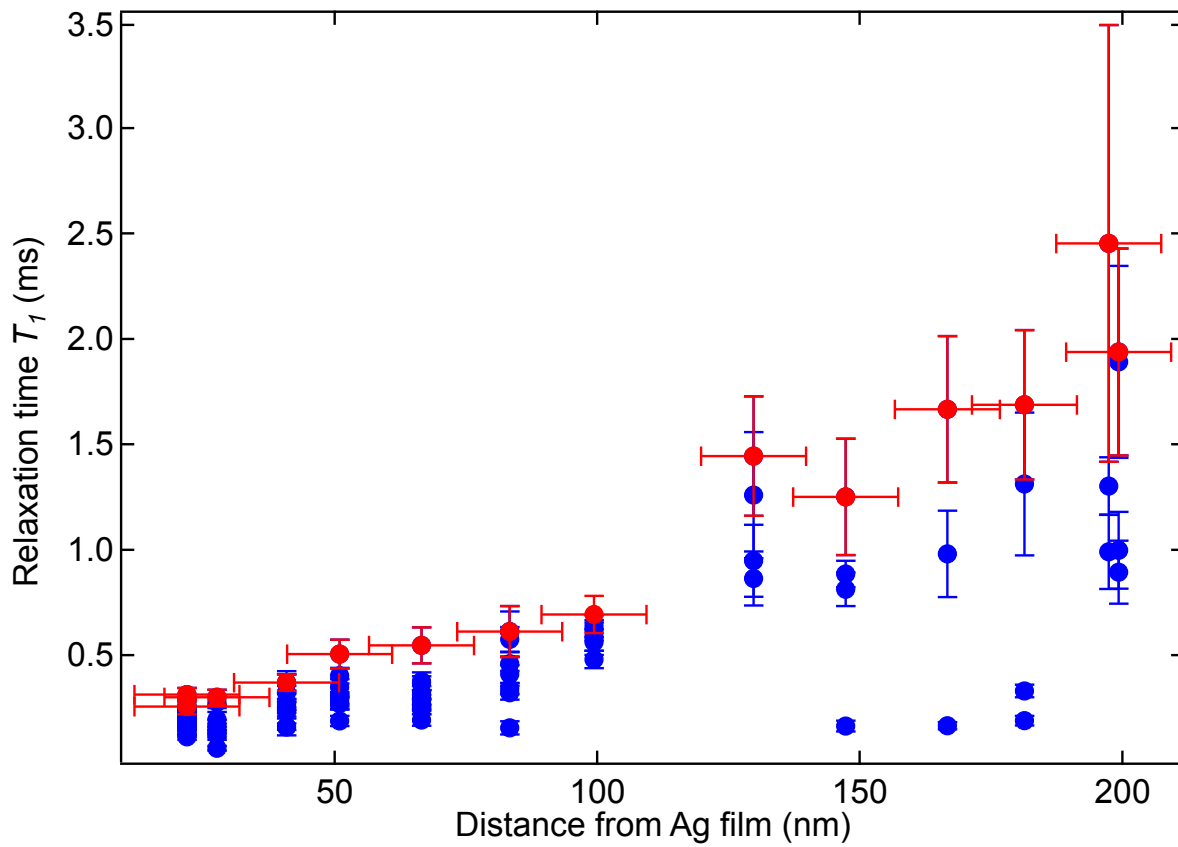


Figure S6:  $T_1$  vs distance to the film, raw data. We vary the distance from NVs to the silver surface via a gradual silica ramp ( $\sim 15$ -200 nm over  $\sim 1.5$  mm), and plot the measured NV  $T_1$  times as a function of distance to the film in each region. The maxima, corresponding to the data shown in Figure 2B of the main text, are plotted in red, and data from all other measured NVs is plotted in blue.

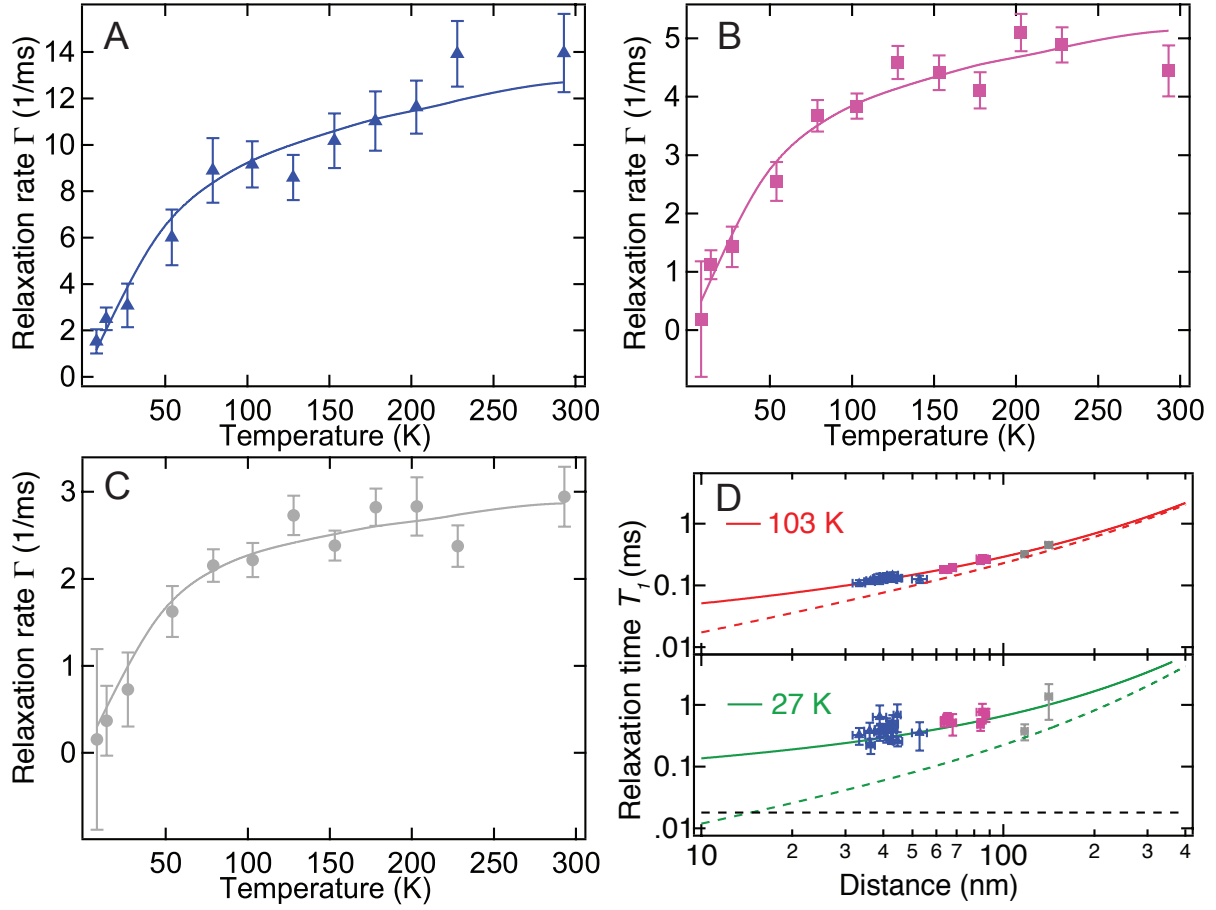


Figure S7: NV decay rates near single-crystal silver with non-local fits. **(A)** Data for an NV in the same region (region A) as the NV in Figure 4B of the main text. The extracted distance from the fit is  $z = 33 \pm 2$  nm. This was the smallest extracted distance we observed for the single-crystal silver measurements. **(B)** Data for an NV in region B, where we expect NVs to be farther away from the silver film than in region A. The extracted distance from the fit is  $z = 88 \pm 2$  nm **(C)** Data for an NV in region C, where we expect the largest separation between the NV and the metal film. The extracted distance is  $z = 141 \pm 4$  nm. **(D)** The same data as in Figure 4D, measured  $T_1$  versus extracted distance for two temperatures, 103 K (top) and 27 K (bottom), color coded by sample region (blue triangles in region A, pink squares in region B, gray circles in region C).

Figure(s)	Number of Averages	Number of points	Wait time range
1C	$2 \times 10^5$	21	0 - 1 ms
1D, S4	$2 \times 10^5$	31	0 - 1.5 ms
2B, S5	$1 \times 10^5$	21	0 - 2 ms
3A	$2 \times 10^5$	11	0 - 2 ms
4B, 4D, S6	$2 \times 10^5$	21	0 - 1.5 ms for $\leq 103$ K 0 - 0.6 ms for $> 103$ K

Table SI: Number of averages, number of measured points, and range of evenly spaced wait times for the  $T_1$  measurements presented in each figure.

Number of NVs	$T_1$
13	$\geq 2$ ms
1	1.2 ms
1	500 $\mu$ s
1	300 $\mu$ s

Table SII:  $T_1$  statistics for 16 of the NVs shown in Figure 4 of the main text (corresponding to the blue triangles in Figure S7D), in the absence of silver.

Region	Mean excited state lifetime
A	8.2 ns
B	12.5 ns
C	13.6 ns

Table SIII: Mean optical excited state lifetimes by spatial region for the NVs show in Figure 4 of the main text and Figure S7D.

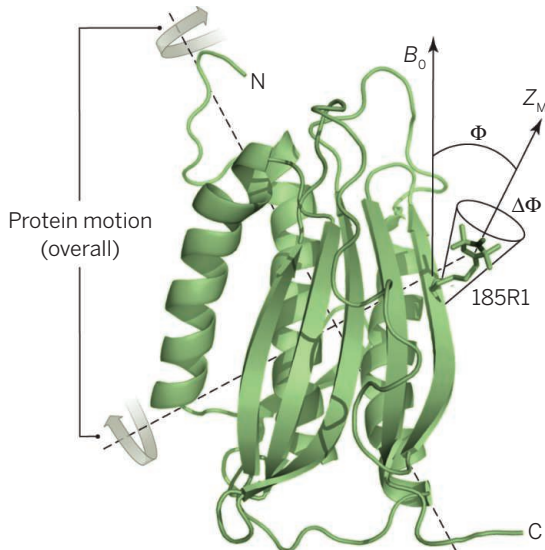
## References and Notes

- [1] M. Lundstrom, *Science* **299**, 210 (2003).
- [2] B. Weber, *et al.*, *Science* **335**, 64 (2012).
- [3] Q. Xu, B. Schmidt, S. Pradhan, M. Lipson, *Nature* **435**, 325 (2005).
- [4] L. Novotny, B. Hecht, *Principles of nano-optics* (Cambridge university press, 2012).
- [5] A. L. Falk, *et al.*, *Nature Physics* **5**, 475 (2009).
- [6] C. Henkel, S. Pötting, M. Wilkens, *Applied Physics B* **69**, 379 (1999).
- [7] Y. Lin, I. Teper, C. Chin, V. Vuletic, *Physical Review Letters* **92**, 050404 (2004).
- [8] M. P. A. Jones, C. J. Vale, D. Sahagun, B. V. Hall, E. A. Hinds, *Physical Review Letters* **91**, 080401 (2003).
- [9] D. Harber, J. McGuirk, J. Obrecht, E. Cornell, *Journal of Low Temperature Physics* **133**, 229 (2003).
- [10] M. Brownnutt, M. Kumph, P. Rabl, R. Blatt, Ion-trap measurements of electric-field noise near surfaces, [arXiv:1409.6572](https://arxiv.org/abs/1409.6572) (2014).
- [11] L. S. Langsjoen, A. Poudel, M. G. Vavilov, R. Joynt, *Physical Review A* **86**, 010301 (2012).
- [12] C. Beenakker, H. van Houten, *Solid state physics* **44**, 228 (1991).
- [13] S. Datta, *Electronic transport in mesoscopic systems* (Cambridge university press, 1997).
- [14] A. C. Bleszynski-Jayich, *et al.*, *Science* **326**, 272 (2009).
- [15] H. Bluhm, N. C. Koshnick, J. A. Bert, M. E. Huber, K. A. Moler, *Physical Review Letters* **102**, 136802 (2009).
- [16] D. Rothfuß, A. Reiser, A. Fleischmann, C. Enss, *Applied Physics Letters* **103**, 052605 (2013).
- [17] L. Childress, *et al.*, *Science* **314**, 281 (2006).
- [18] J. Maze, *et al.*, *Nature* **455**, 644 (2008).
- [19] G. Balasubramanian, *et al.*, *Nature* **455**, 648 (2008).
- [20] J. Tetienne, *et al.*, *Science* **344**, 1366 (2014).

- [21] E. Schäfer-Nolte, *et al.*, Tracking Temperature Dependent Relaxation Times of Individual Ferritin Nanomagnets with a Wide-band Quantum Spectrometer, [arXiv:1406.0362](https://arxiv.org/abs/1406.0362) (2014).
- [22] M. Pelliccione, B. A. Myers, L. Pascal, A. Das, A. C. Bleszynski Jayich, Two-dimensional nanoscale imaging of gadolinium spins via scanning probe relaxometry with a single spin in diamond, [arXiv:1409.2422](https://arxiv.org/abs/1409.2422) (2014).
- [23] Materials and methods are available as supporting material on *Science* Online.
- [24] T. H. Taminiau, J. Cramer, T. van der Sar, V. V. Dobrovitski, R. Hanson, *Nature Nanotechnology* **9**, 171 (2014).
- [25] A. A. Baski, H. Fuchs, *Surface Science* **313**, 275 (1994).
- [26] J. H. Park, *et al.*, *Advanced Materials* **24**, 3988 (2012).
- [27] G. W. Ford, W. Weber, *Physics Reports* **113**, 195 (1984).
- [28] N. W. Ashcroft, N. D. Mermin, *Solid State Physics* (Holt, Rinehart and Winston, 1976).
- [29] P. Maher, *et al.*, *Science* **345**, 61 (2014).
- [30] L. Faoro, L. B. Ioffe, *Physical Review Letters* **100**, 227005 (2008).
- [31] S. M. Anton, *et al.*, *Physical Review Letters* **110**, 147002 (2013).
- [32] L. S. Langsjoen, A. Poudel, M. G. Vavilov, R. Joynt, *Physical Review B* **89**, 115401 (2014).
- [33] A. Jarmola, V. M. Acosta, K. Jensen, S. Chemerisov, D. Budker, *Physical Review Letters* **108**, 197601 (2012).
- [34] S. Pezzagna, B. Naydenov, F. Jelezko, J. Wrachtrup, J. Meijer, *New Journal of Physics* **12**, 065017 (2010).

Once this had been accomplished, the race was on to image single proteins with the NV center. The first major milestone on this path was the detection of small volumes of nuclear spins, close to those volumes previously achieved by MRFM, except at room temperature. This was done by two groups simultaneously (7, 8). In the latter work, the technique was pushed a step farther by interrogating the nuclear spin ensemble to give information on their local environment. By applying these techniques to single proteins, low-resolution images should be possible. However, ultimately atomic-scale resolution image of proteins are needed, at least in the reaction centers. This requires the ability to locate individual nuclei.

In the past year, detection and imaging of near-single nuclear spins outside the diamond lattice was reported (9). Here, four



**See it move.** Dynamics of the spin label attached to the MAD2 protein.  $B_0$  is the external magnetic field,  $Z_M$  is the spin label quantization axis, and  $\Delta\Phi$  is the angular range of motion.

silicon nuclei were observed on a specially designed glass-like coating placed on the diamond surface. This work was important because it proved that the magnetic noise produced by unpaired electrons at or near the diamond surface could be overcome, at least in principle. Until then, this magnetic noise was a roadblock that made many question whether a single external nuclear spin could ever be detected by a NV center.

Although the earlier studies proved that it is possible to greatly reduce the numbers of troublesome diamond surface spins, it has so far not been possible to eliminate them completely. However, very recently it has been shown that these few remaining surface spins can often be stable enough to use as a resource—namely, making them into “reporter” spins to image single nu-

clei in their immediate environment (10); a single proton bound to the diamond surface was imaged.

However, what is ultimately needed is a way to deploy reporter spins that are not limited to the diamond surface but that can be detected at long range and selectively placed at critical locations in a protein where they can sense conformation changes. It is exactly this lofty goal that has now been accomplished by Shi *et al.* (see the figures). A nitroxide spin label is anchored to a region of interest on a single protein. Each nitroxide has a single unpaired electron spin that is capable of detecting nearby nuclei by a process known as the hyperfine interaction. The nitroxide reporter spin is ~10 nm from the NV and ~5 nm beyond the diamond surface, far enough to image remote parts of the protein. Not only were Shi *et al.* able to image the

location of the reporter electron spin, they could also detect a single nuclear spin nearby. Furthermore, by analyzing the hyperfine spectrum of this nuclear spin, the approximate angle of its preferred axis relative to an applied magnetic field could be deduced [see figure 3A in (2)]. From this orientation information, they were able to infer the approximate angular range of motion of that part of the protein, which is a measure of protein flexibility and/or conformation changes. More important, the average angular motions were found to occur on time scales relevant for biological interactions.

In the future, it will be necessary to monitor far more than one nuclear spin in the protein, and so better reporter spin labels are needed. Specifically, they must have longer spin coherence times to achieve longer-range nuclear spin imaging, and they must be photostable to the light used to interrogate the NV center. Finally, to image proteins in living cells, the bulk diamond used in these experiments must be replaced by a nanodiamond with similar NV magnetic sensitivity. ■

#### REFERENCES

1. J.S. Valastyan, S. Lindquist, *Dis. Model. Mech.* **7**, 9 (2014).
2. F. Shi *et al.*, *Science* **347**, 1135 (2015).
3. C.L. Degen, M. Poggio, H.J. Mamin, C.T. Rettner, D. Rugar, *Proc. Natl. Acad. Sci. U.S.A.* **106**, 1313 (2009).
4. G. Balasubramanian *et al.*, *Nature* **455**, 648 (2008).
5. J.R. Maze *et al.*, *Nature* **455**, 644 (2008).
6. B. Grotz *et al.*, *New J. Phys.* **13**, 055004 (2011).
7. T. Staudacher *et al.*, *Science* **339**, 561 (2013).
8. H.J. Mamin *et al.*, *Science* **339**, 557 (2013).
9. C. Müller *et al.*, *Nat. Commun.* **5**, 4703 (2014).
10. A. Ajoy *et al.*, *Phys. Rev. X* **5**, 011001 (2015).

10.1126/science.aaa7440

## QUANTUM MECHANICS

# Look but don't touch the metals

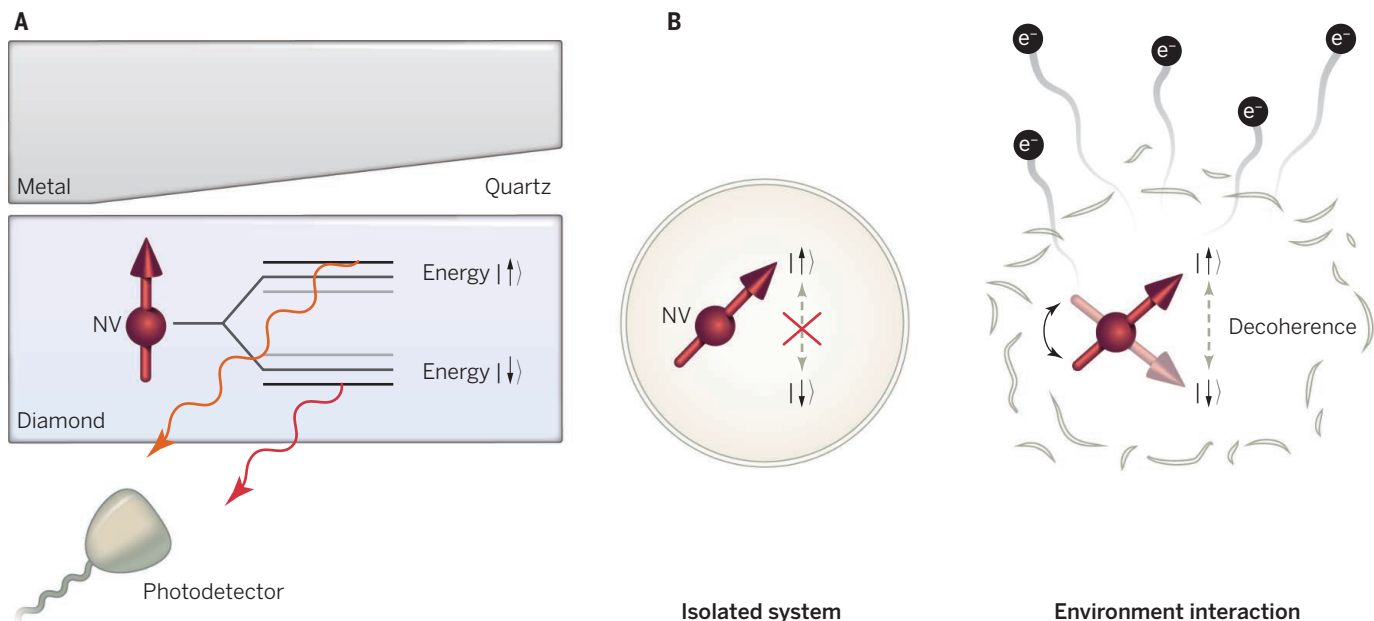
Nitrogen-vacancy defects in diamond can probe metallic conductivity at a distance

By Liam P. McGuinness<sup>1,2</sup>  
and Fedor Jelezko<sup>1,3</sup>

**M**etallic conductivity is a familiar phenomenon, but metals can display surprising and exotic behavior, such as superconductivity and the quantum Hall effect. Advances in nanotechnology have led to new questions about how metallic conductivity might change in structures with dimensions approaching a few atoms. On page 1129 of this issue, Kolkowitz *et al.* (1) provide us with another tool for answering these questions: a magnetic sensor based on atomic defects in diamond.

Conductivity measurements have historically used sensors similar to an electrical multimeter, in which electrical contacts are placed across a device to measure its properties. The approach is akin to many people's first exploratory investigations of a new toy—pick it up and touch it. However, like delicate toys that can be damaged by even the most careful handling, miniaturized electrical devices are now at the point where the measuring contacts disrupt the material characteristics. For this reason, “look but don't touch” methods such as superconducting quantum interference devices (SQUIDs) and cold atomic gases have been developed. Instead of measuring resistance and conductivity via electrical contact to the sample, the magnetic field produced by electron motion is observed from a distance.

One criticism of these techniques has been their inability to measure nanometer-sized devices, because most are limited to the micrometer or millimeter scale. Recently, single dopants in diamond were proposed for experiments in nanoscale magnetic sensing (2, 3). Optically active dopants often carry ground-state spin, and for the nitrogen-vacancy (NV) color center in particular, the spin state can be coupled to photons and achieve ultrasensitive optical readout of the spin levels (4, 5). As spin en-



**A light touch.** (A) Single defects in diamond known as NV centers are placed at the surface and separated from the metal layer with a gradient quartz spacer, tens of nanometers in thickness. The spin energy levels of the NV center can be monitored optically, and their response to magnetic fields (which can increase the energy gap) used as a sensitive magnetometer. (B) Rather than measuring the energy levels directly, the relaxation rate between sublevels provides information about the external environment. Well-isolated quantum systems have low relaxation rates because the environment does not provide enough energy to flip the NV spin. Bringing a noisy environment (such as moving electrons) near the NV center induces quantum decoherence and can be used to monitor dynamics in order to differentiate diffusive electron motion from ballistic motion.

ergy levels depend on the external magnetic field (known as the Zeeman effect), this technique provides a precise magnetic sensor with little more experimental setup than an optical microscope and a piece of diamond (see the figure, panel A). In (1), single NV centers were implanted in diamond with an ion beam with a well-defined energy. Careful control of the distance to the metal layer is a key point in the experiment. Kolkowitz *et al.* controlled distance by introducing a wedged quartz spacer between the diamond and metal, and boosted magnetic sensitivity by using a decoherence microscopy technique (6). Instead of measuring the energy of the spin levels directly, they monitored the relaxation rate between levels.

This approach takes advantage of the exquisite sensitivity of quantum systems to their environment. Quantum decoherence, resulting from interaction with the external environment, is the bane of many physicists' existence, and is generally avoided at all costs. Indeed, this pernicious interaction is one reason quantum computers are so difficult to build, and is also why quantum effects are not seen in everyday life. However, Kolkowitz *et al.* turn the paradigm on its head to use quantum decoherence for their benefit: Because decoherence

is caused by the environment, it can be used to provide information about the local surroundings (see the figure, panel B). Careful monitoring of the relaxation rates unraveled details of electron transport in a nearby metal layer. Clear differences for the cases of diffusive motion of electrons in polycrystalline silver (ohmic behavior) and ballistic motion of electrons in single-crystal films were demonstrated.

So how little "touch" is imparted onto the investigated metal by the team's noncontact method? Electrical isolation is ensured by the quartz layer separating the silver from the sensor, whereas physical contact can be avoided completely by fixing the diamond to a scanning tip (7). More concerning might be the unavoidable "back-action" that measurements produce in quantum physics. Kolkowitz *et al.* address this issue by measuring what is an essentially classical system, where the quantum back-action is negligible. The field produced by their single-spin sensor is completely swamped by the many thousands of electrons in the metal. However, at low temperatures, where quantum effects become relevant, quantum interaction between NV ensembles and superconducting resonators has indeed been demonstrated (8, 9).

The readout laser is perhaps the most invasive part of the measurement protocol. Illumination of metals with light can produce substantial changes in conductivity and can even lead to ejection of electrons

(the photoelectric effect). However, all of the information was gathered in the dark, when the laser was turned off and stored in the NV state. A short laser pulse was applied only at the end of the measurement to read out the sensor. Laser illumination can actually be used as a resource, in concert with diamond-based readout, to manipulate magnetic properties at the nanoscale, as shown recently (10).

The work of Kolkowitz *et al.* provides researchers with another tool for probing the importance of dimensionality, geometry, and topology on conductivity at the nanoscale. It is an important complement to well-established electrical readout techniques (11) and joins a growing repertoire of diamond sensors being applied to a diverse range of materials. As far as metals and conductivity are concerned, diamonds are nearly untouchable. ■

#### REFERENCES

1. S. Kolkowitz *et al.*, *Science* **347**, 1129 (2015).
2. A. Gruber *et al.*, *Science* **276**, 2012 (1997).
3. B. M. Chernobrod, G. P. Berman, *J. Appl. Phys.* **97**, 014903 (2005).
4. G. Balasubramanian *et al.*, *Nature* **455**, 648 (2008).
5. J. R. Maze *et al.*, *Nature* **455**, 644 (2008).
6. J. H. Cole, L. C. L. Hollenberg, *Nanotechnology* **20**, 495401 (2009).
7. P. Maletinsky *et al.*, *Nat. Nanotechnol.* **7**, 320 (2012).
8. Y. Kubo *et al.*, *Phys. Rev. Lett.* **105**, 140502 (2010).
9. X. Zhu *et al.*, *Nature* **478**, 221 (2011).
10. J.-P. Tetienne *et al.*, *Science* **344**, 1366 (2014).
11. A. Brenneis *et al.*, *Nat. Nanotechnol.* **10**, 135 (2015).

<sup>1</sup>Institute of Quantum Optics, Ulm University, Ulm, D-89069 Germany. <sup>2</sup>School of Physics, University of Melbourne, Melbourne, 3010 Australia. <sup>3</sup>Center for Integrated Quantum Science and Technology (IQST), Ulm University, Ulm, D-89069 Germany. E-mail: fedor.jelezko@uni-ulm.de

*This copy is for your personal, non-commercial use only.*

**If you wish to distribute this article to others**, you can order high-quality copies for your colleagues, clients, or customers by [clicking here](#).

**Permission to republish or repurpose articles or portions of articles** can be obtained by following the guidelines [here](#).

***The following resources related to this article are available online at [www.sciencemag.org](http://www.sciencemag.org) (this information is current as of March 9, 2015):***

**Updated information and services**, including high-resolution figures, can be found in the online version of this article at:

<http://www.sciencemag.org/content/347/6226/1073.full.html>

A list of selected additional articles on the Science Web sites **related to this article** can be found at:

<http://www.sciencemag.org/content/347/6226/1073.full.html#related>

This article **cites 11 articles**, 2 of which can be accessed free:

<http://www.sciencemag.org/content/347/6226/1073.full.html#ref-list-1>

This article appears in the following **subject collections**:

Physics

<http://www.sciencemag.org/cgi/collection/physics>